



Norwegian University of  
Science and Technology

# Nickel Promoted Cobalt Fischer- Tropsch Catalysts

Effect of Nickel on reducibility and Cobalt dispersion

**Vegar Evenrud**

Chemical Engineering and Biotechnology

Submission date: February 2012

Supervisor: Magnus Rønning, IKP

Co-supervisor: Georg Voß, IKP



## Abstract

The effect of nickel promotion in cobalt Fischer-Tropsch catalysts towards reducibility and cobalt dispersion was investigated. A series of catalysts loaded with 20% Co and 0-10% Ni on  $\gamma\text{-Al}_2\text{O}_3$  were impregnated by the incipient wetness method and calcinated in two steps: First with Ni, then Co.

Reducibility was studied with TPR and compared with data from in-situ XRD and TGA. Particle sizes and dispersion was studied with chemisorption, in-situ and ex-situ XRD. Sintering of cobalt particles during reduction and at elevated temperatures was also studied with in-situ XRD.

Promotion with Ni was shown to decrease the reduction temperature of the  $\text{Co}_3\text{O}_4 \rightarrow \text{CoO}$  reduction step, while not influencing the second reduction step towards metallic Co. Ni promotion was also shown to increase dispersion by inhibiting sintering of Co particles both during the second reduction step  $\text{CoO} \rightarrow \text{Co}$ , and at elevated temperatures.

## Abstrakt

Effekten av nikkelpromosjon på koboltbaserte Fischer-Tropsch-katalysatorer med hensyn til reduserbarhet og dispersjon av kobolt ble undersøkt. En serie av katalysatorer med et metallinnhold på 20% Co og 0-10% Ni på  $\gamma\text{-Al}_2\text{O}_3$ -bærere ble framstilt ved impregnering og kalsinering i to omganger: Først med Ni, så med Co.

Katalysatorenes reduserbarhet ble undersøkt ved temperaturprogrammert reduksjon og sammenliknet med data fra in-situ røntgendiffraksjon og termogravimetrisk analyse. Partikkelstørrelser og dispersjon ble undersøkt ved kjemisorpsjon, in- og ex-situ røntgendiffraksjon. Sintring av koboltpartikler under reduksjon, samt ved høye temperaturer ble også undersøkt med in-situ røntgendiffraksjon.

Promosjon med Ni viste seg å senke reduksjonstemperaturen for reduksjonstrinnet  $\text{Co}_3\text{O}_4 \rightarrow \text{CoO}$ , mens det siste reduksjonstrinnet til metallisk Co ikke ble påvirket. Promosjon med Ni viste seg også å øke dispersjonen ved å motvirke sintring av Co-partiklene under det andre reduksjonstrinnet  $\text{CoO} \rightarrow \text{Co}$ , samt ved høye temperaturer.



# Preface

This thesis is submitted for the degree *sivilingeniør*/Master of Science and concludes the five-year *Industriell kjemi og bioteknologi* study programme at the Norwegian University of Science and Technology (NTNU). The work for this thesis has been carried out at the petrochemistry and catalysis group at the Department of Chemical Engineering in the period September 2011 - January 2012. The thesis is also based upon my specialization project carried out at the same institution in the period April - June 2011. Professor Magnus Rønning and Ph.D. candidate Georg Voß have been my supervisors during both works.

I want to thank all the people at the Department of Chemical Engineering and the Faculty of Natural Sciences and Technology that have helped me with both small and big issues during my work. I would in particular mention: My supervisors Magnus Rønning and Georg Voß for their help and assistance during my work. Sivilingeniør Inger Marie Bjørnevik and staff engineer Karin Wiggen Dragsten at the department of chemical engineering for help with various experimental set-ups. Dr. Julian Tolchard at the Department of Materials Science and Engineering for discussions about, and assistance with the XRD and BET. Dr. Rune Lødeng at SINTEF Materials and Chemistry for help with the TPR. I also want to thank Anne Kristine Evenrud, Gunvor Evenrud, Trine Aabakken and Maren Sofie Løfsgård for proofreading this document.

Trondheim,  
February 5th, 2012

A handwritten signature in cursive script that reads "Vegar Evenrud". The signature is written in dark ink on a white background.



# Contents

<b>Abstract</b>	<b>i</b>
<b>Preface</b>	<b>iii</b>
<b>Contents</b>	<b>v</b>
<b>1 Introduction</b>	<b>1</b>
1.1 Historical background . . . . .	2
1.2 Reactions . . . . .	3
1.3 Process . . . . .	5
1.4 Product . . . . .	6
1.5 Catalysts . . . . .	6
1.6 Promoters . . . . .	7
1.7 Nickel as a promoter . . . . .	9
1.8 Catalyst preparation . . . . .	11
1.9 Temperature programmed reduction . . . . .	12
1.10 Thermal gravimetric/Differential thermal analysis . . . . .	13
1.11 Mass spectrometry . . . . .	13
1.12 X-ray diffraction . . . . .	13
1.13 Physisorption . . . . .	15
1.14 Chemisorption . . . . .	16

<b>2</b>	<b>Experimental work</b>	<b>19</b>
2.1	Catalyst preparation . . . . .	19
2.2	Temperature programmed reduction . . . . .	21
2.3	TGA/DTA/MS . . . . .	22
2.4	Physisorption . . . . .	23
2.5	Chemisorption . . . . .	23
2.6	X-ray diffraction . . . . .	24
2.7	Risk assessment . . . . .	26
<b>3</b>	<b>Results and discussion</b>	<b>27</b>
3.1	Physisorption . . . . .	27
3.2	Ex-situ XRD . . . . .	28
3.3	In-situ XRD . . . . .	30
3.4	TPR . . . . .	36
3.5	TGA/DTA/MS . . . . .	38
3.6	Chemisorption . . . . .	40
3.7	Effect of preparation method . . . . .	40
3.8	Effect on reducibility . . . . .	42
3.9	Effect on dispersion . . . . .	43
<b>4</b>	<b>Conclusion</b>	<b>45</b>
	<b>Nomenclature</b>	<b>47</b>
	<b>Bibliography</b>	<b>49</b>
<b>A</b>	<b>Peak fitting of <math>\gamma</math>-Al<sub>2</sub>O<sub>3</sub> supports in TOPAS</b>	<b>55</b>
<b>B</b>	<b>Examples of calculations</b>	<b>59</b>

<i>CONTENTS</i>	vii
<b>C Additional data and results</b>	<b>65</b>
<b>D Risk assesment</b>	<b>77</b>



# Chapter 1

## Introduction

The Fischer-Tropsch synthesis is a method of synthetic hydrocarbon production that has gained interest as an alternative source for transportation fuels as the world's reserves of easily accessible oil are shrinking [1]. While still a somewhat expensive process, R&D efforts have previously improved this technology towards commercialization. Noble metal promotion of cobalt catalysts used in the Fischer-Tropsch synthesis has been shown to be beneficial to catalyst activity. Because of the high prices and/or low availability of these promoters, development of catalysts based on cheaper promoters could decrease the operation costs of a Fischer-Tropsch plant and make the technology more competitive [2]. Rytter et al. [3] has investigated the possibility of using nickel as an inexpensive substitute for the rhenium promoters in these catalysts.

The aim of this thesis is to investigate how promotion with nickel affects reducibility and dispersion of cobalt catalysts. The catalysts were synthesized as a part of the work with this thesis and characterized using temperature programmed reduction, chemisorption and both in-situ and ex-situ x-ray diffraction. Thermal gravimetric analysis and physisorption (BET) were also used in some extent. The analyses have mostly focused on catalysts where cobalt was added to nickel catalysts. Some comparison has also been done with co-impregnated catalysts and catalysts where nickel was added to cobalt catalysts.

The Fischer-Tropsch synthesis and catalysts are treated in general in section 1.1-1.5 of this chapter, while promotion with and without nickel are treated

in section 1.6-1.7. Section 1.8-1.14 describes the background of the different experimental methods used, while the actual experimental work is described in chapter 2. Chapter 3 presents and discusses the findings of this work.

## 1.1 Historical background

The Fischer-Tropsch synthesis has its origin in inter-war period Germany. When petroleum emerged as an important fuel for transportation in the early twentieth century, Germany found itself dependent on oil import as it had few sources of petroleum inside its own territories. In order to make themselves less dependent of this import, huge efforts were put into the development of coal to liquids (CtL) technologies to utilize Germany's rich coal deposits. Most prominent of these was the Bergius process. In 1923, Franz Fischer (1877-1947) and Hans Tropsch (1889-1935) discovered the Fischer-Tropsch synthesis in which coal derived synthesis gas was converted to hydrocarbons over a cobalt or iron catalyst. Production at the first Fischer-Tropsch plant started in 1936, and eight more were constructed until the end of world war II. All plants from this era did utilize the cobalt catalyst [4, 5].

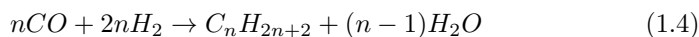
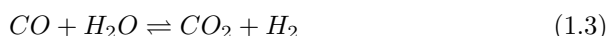
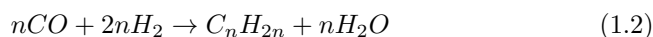
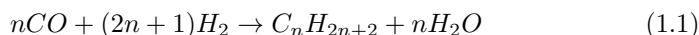
In the period following the war, the Fischer-Tropsch process was studied further, mainly in the US. Fischer-Tropsch based gas to liquids (GtL) technology and the iron catalyst was developed during this period, and in total three plants were constructed. However, the Fischer-Tropsch process was immature and uncompetitive to fuels made of petroleum and the plants was shut down during the 1950s [4]. In South Africa, the situation was somewhat similar to that of inter-war Germany: The country was dependent on oil import while rich in coal resources and distrusted in the international community due to its racial segregation policy. They started building Fischer-Tropsch plants through the company SASOL, and three plants were constructed during the period 1955-1982. All of these plants used iron catalysts, but utilized somewhat different process designs. The activity around these plants has made South Africa a leading country in Fischer-Tropsch technology [5, 6].

Today, outlook of increased oil prices and the possibility of developing remote gas fields have given the Fischer-Tropsch technology a renewed interest. Commercial plants are operated by companies SASOL, Shell and PetroSA, while

ExxonMobil, BP, ConocoPhillips, Eni and Statoil are examples of companies that are developing and testing the technology at pilot scale [5].

## 1.2 Reactions

The overall reactions of the Fischer-Tropsch synthesis are listed below [6]:



Reactions 1.1 and 1.2 are the main reactions producing hydrocarbons, while reaction 1.4 is producing various oxygenates like alcohols, aldehydes, ketones and carboxylic acids. The reactions are highly exothermic with a heat of reaction of 165 kJ/mol per  $[-CH_2-]$  repeat unit [1]. The reaction producing paraffins (1.1) are the most extensive of the reactions and also the most desired in means of fuel production. The extent of olefin production (1.2) is usually in the range of 5-15% percent for a cobalt catalyzed reaction, while oxygenates production (1.4) is normally lower than 6%. The reactions are very selective towards linear hydrocarbons, and branched compounds usually constitute for less than 5% of the product [1]. The water-gas shift reaction (WGS, 1.3) affects the composition of the feed and takes place at iron based Fischer-Tropsch catalysts, or in a dedicated reactor. Coke formation through the Boudouard reaction (1.5) is a major cause of catalyst deactivation [1].

The hydrocarbons are formed through a chain growth polymerization mechanism where CO monomers are added to a growing hydrocarbon chain at an active site of the catalyst. According to Flory's assumption, the reactivity of the growing hydrocarbon chain is independent of the chain length [7]. The probability of a monomer to be added to the growing chain is thus assumed to be constant and described as  $\alpha$ . The probability for a chain to stop growing and desorb instead is then  $1-\alpha$ .  $\alpha$  can be described with the rate constants of

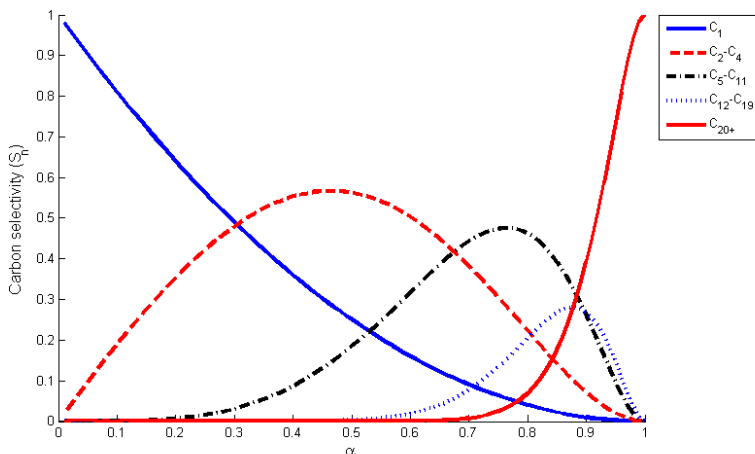


Figure 1.1: *Selectivity towards different ranges of chain lengths as a function of  $\alpha$ . Based on figure by Holmen [8].*

chain propagation ( $k_p$ ), and chain termination ( $k_t$ ) [8]:

$$\alpha = \frac{k_p}{k_p + k_t} \quad (1.6)$$

The probability to make a hydrocarbon chain of length  $n$  is then :

$$p_n = p_0 \alpha^{n-1} (1 - \alpha) \quad (1.7)$$

The concept of carbon selectivity ( $S_n$ ) can be used to describe the distribution of chain lengths in the product.  $S_n$  is describing the amount of CO monomers that have been converted into a chain of length  $n$  as a fraction of CO monomers converted in total [8]:

$$S_n = \frac{np_n}{\sum_{n=1}^{\infty} np_n} = \frac{n\alpha^n(1-\alpha)^2}{\alpha} \quad (1.8)$$

Figure 1.1 illustrates how  $\alpha$  is influencing the selectivity towards different ranges of chain lengths. A high selectivity towards the wax fraction ( $C_{20+}$ ) is often desired. Increasing the value of  $\alpha$  is then an important goal in catalyst development. The literature states that the value of  $\alpha$  is limited upwards to 0.94 for

cobalt catalysts and 0.95 for iron catalysts [9]. While the value of  $\alpha$  is mainly determined by the catalyst properties, it does also vary with reaction conditions and feed composition. An increase in the temperature will for example lower the value of  $\alpha$ , while  $\alpha$  increases with increased pressure for cobalt catalysts (but to little degree for iron catalysts) [10]. It should be noticed that equation 1.7 shows that while a high carbon selectivity will cause a high weight fraction of heavy components (long chains), light components will still have the highest mole fractions. The exact reaction mechanism at the active site has however been disputed since the discovery of the Fischer-Tropsch synthesis [8].

## 1.3 Process

The Fischer-Tropsch process can basically be divided into three main steps: Production of synthesis gas, Fischer-Tropsch synthesis and product upgrade. Coal or natural gas are the most common feedstocks for synthesis gas production, while biomass are also studied as a possible feedstock. Solid feedstocks are converted into synthesis gas in a gasifier, while steam- or autothermal reformers are used for natural gas [6]. The synthesis gas is cleaned for unwanted components before fed to the Fischer-Tropsch reactor. Unwanted components may be catalyst poisons like sulfur, or sometimes also inhibiting compounds like water and carbon dioxide. The synthesis gas composition may also be adjusted with a WGS reactor [6].

The Fischer-Tropsch synthesis itself exists in two different versions: A high temperature process (HTFT) applying iron catalysts in a fluidized bed reactor at 300-350 °C and 20-40 bar, and a low temperature process (LTFT) applying either cobalt or iron catalysts in a fixed bed or slurry reactor at 200-240 °C and 20-45 bar [9]. Because the Fischer-Tropsch synthesis gives a wide product distribution in the means of chain lengths, the process is often optimized to yield a high fraction of long hydrocarbon chains (wax fraction) and minimizing the amount of light fraction products like methane. The wax fraction is converted into transport fuel in the product upgrade process. The product upgrade is basically an oil refinery where the Fischer-Tropsch product is separated in a fractionator and converted into fuels by hydrocracking and hydrotreating [1, 6, 11]. The synthesis gas production and Fischer-Tropsch synthesis are highly exothermic, thus process integration and utilization of excess heat will

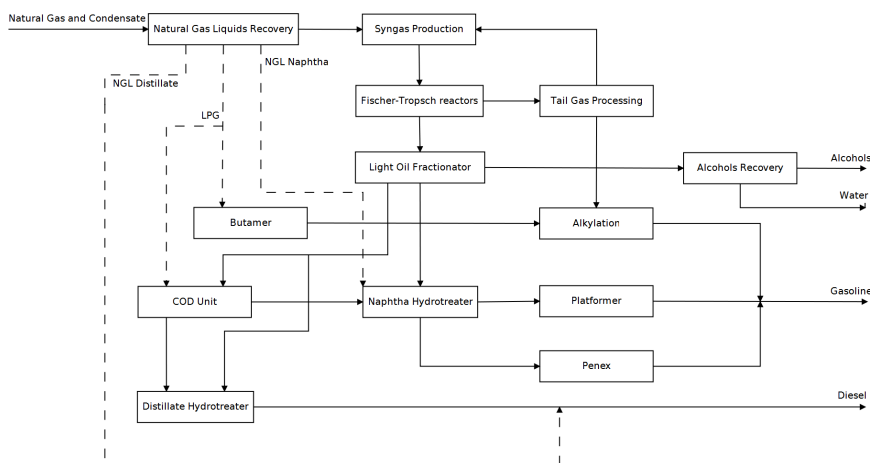


Figure 1.2: *Block diagram of the PetroSA GtL plant in Mossel Bay, South Africa. Based on a figure by Dancurat et. al. [5]*

have a considerable impact on the profitability of the plant [11]. Figure 1.2 shows an example of a Fischer-Tropsch plant.

## 1.4 Product

The hydrocarbons made through the Fischer-Tropsch synthesis are mainly unbranched paraffins that are virtually free of aromatics. As a result of these properties, they have a high cetane number and are well suited as a clean burning fuel for diesel engines. The product is also free of sulfur, metals, and nitrogen containing compounds, making the Fischer-Tropsch diesel more environmentally friendly than diesel derived from petroleum. Compared with methanol, which is another fuel produced from synthesis gas, the Fischer-Tropsch diesel is compatible with existing engines and infrastructure and can without problems be used as a fuel alone or blended with other diesel fuels [1, 10].

## 1.5 Catalysts

All group VIII transition metals can be used to catalyze the hydrogenation of carbon monoxide. Most of them are however unsuitable due to high costs, low

Table 1.1: Comparison of iron and cobalt catalysts. Taken from Khodakov et al. [9].

Catalyst	Iron	Cobalt
Cost	Less expensive	More expensive
Deactivation	Lower resistance to deactivation	Higher resistance to deactivation
Activity at low conversion	Comparable	
Productivity at high conversion	Lower(water has inhibiting effect)	Higher (water has less inhibiting effect)
Maximum value of $\alpha$	0.95	0.94
WGS activity	Significant	Unsignificant (higher at high conversions)
Maximum sulfur content	< 0.2 ppm	< 0.1 ppm
Flexibility towards reaction conditions	Flexible	Less flexible
H <sub>2</sub> :CO-ratio	0.5-2.5	~ 2
Attrition resistance	Bad	Good
Olefin selectivity	Higher	Low
Applied in which process	LTFT/HTFT	LTFT

activity or poor selectivity towards heavy fractions [9, 12]. However, iron and cobalt are the only of these metals that are applicable for industrial application. Nickel does also show high activity, but due to its poor selectivity toward heavy fractions, it is normally used as a methanation catalyst [9]. A comparison between the iron and cobalt catalysts is shown in table 1.1. Cobalt catalysts normally use metal oxides like alumina, silica and titania as support materials with metal loadings in the range of 10-30 wt%. Cobalt catalysts are considered to be a good alternative for low temperature GtL processes since natural gas gives a synthesis gas H<sub>2</sub>:CO-ratio close to 2 [1]. The rest of this thesis will focus on cobalt catalysts only.

## 1.6 Promoters

Cobalt Fischer-Tropsch catalysts can be promoted with noble metal and/or metal oxide promoters in order to manipulate catalyst properties. Noble metals are often applied in loadings of 0.05-0.5%, while metal oxide loadings are in the range of 1-10% [1, 2].

### Noble metals

Noble metals ruthenium, rhenium, platinum and palladium have all been shown to have a positive effect on cobalt catalysts. In general, increased catalyst

activity has been shown for all of them, while their effect on the selectivity are more varying: Platinum and palladium are decreasing the selectivity towards heavy fractions while ruthenium has no effect on the selectivity. Whether rhenium increases the selectivity toward heavy fractions or not is disputed [1, 2, 9]. Cobalt reducibility and both the degree of reduction and a decrease of reduction temperatures are promoted by noble metals. The reduction step from CoO to cobalt metal (eq. 1.10) is promoted by all of the noble metals, while the reduction step from Co<sub>3</sub>O<sub>4</sub> to CoO (eq. 1.9) is promoted by all of them except for rhenium. This effect is assumed to be caused by hydrogen spillover from reduced noble metal particles to the cobalt oxides [1, 13]. The noble metals also increase cobalt dispersion, but have no effect on cobalt particle sizes. The increase in dispersion is therefore assumed to be caused by the increased degree of reduction. Since the turn over frequency (TOF) is known to be constant, increased activity is assumed to be caused by the increased number of active sites due to higher dispersion [1, 2, 13]. Ruthenium has also been shown to inhibit the formation of cobalt-support oxides (that is not catalytic active) [2]. The effect of noble metals towards deactivation is disputed: They are normally assumed to have no effect on deactivation, but there are also some claims that platinum and rhenium could increase deactivation at alumina supported catalysts [2]. Due to the low metal loading of noble metals, they have no effect on the mechanical properties of the catalysts [2].

The noble metals are however expensive and rare, their relative prices compared with cobalt are 1:70:200:650 in the order: Co:Re:Ru:Pt [2]. The annual production of platinum and palladium are around 200 tons, while the production of rhenium and ruthenium are respectively  $\sim 45$  and  $\sim 2$  tons. The low production capacity of those metals makes platinum and palladium the only noble metals accessible enough to be used in an industrial scale process plant [2].

## Metal oxides

Various metal oxides are known to influence the cobalt catalysts. Zirconia (ZrO<sub>2</sub>) promotes both catalyst activity and selectivity towards heavy fractions. ZrO<sub>2</sub> promotes the reducibility, but do also cause bigger cobalt particles. The increased number of active seats available due to the increased degree of reduction does however counter the increased particle size. The zirconia is also

inhibiting the formation of cobalt-support oxides, but does however decrease the mechanical strength of the catalyst [9].

Lanthanum oxide ( $\text{La}_2\text{O}_3$ ) does not affect the catalyst activity at low loadings, but does increase the selectivity towards heavy fractions. It does however decrease activity at high loadings [9].

Manganese oxide ( $\text{MnO}$ ) does increase both cobalt dispersion and activity through increased TOF at low loadings. At low loadings it promotes the selectivity towards heavy fraction, but does also increase the olefin selectivity at higher loadings. It does however decrease the catalyst's reducibility [9].

## 1.7 Nickel as a promoter

As mentioned in section 1.6, rhenium shows good properties as a promoter, but is considered unfit for large scale industrial utilization due to its rarity. An inexpensive substitute is therefore necessary. Nickel is such a metal from the same group as palladium and platinum. Because of its high selectivity towards light fractions, it has traditionally been deemed unfit and the available literature about nickel as a Fischer-Tropsch promoter is scarce.

Ishihara and Horiuchi et al. [14, 15, 16, 17] studied bimetallic cobalt-nickel catalysts on silica and titania supports during the late 1980's. Their catalysts were made by coimpregnation and the resulting metal particles was identified as a cobalt-nickel alloy. They found that nickel improved activity and selectivity towards heavy fractions. This effect was most prominent for alloys with equal amounts of cobalt and nickel. However, the selectivity toward olefins and oxygenates was also increased. Nickel was also shown to promote iron catalysts, but addition of iron to the cobalt-nickel catalyst did decrease its activity and selectivity. The reducibility of the catalyst was increased compared with a cobalt only catalyst, while only small variations in the metal particle size was observed. The same trends were shown for titania supports. The positive effect of nickel was explained as an effect of an increase in hydrogen adsorption, since carbon monoxide is the dominating adsorbate at the catalyst surface. Cobalt-nickel catalysts was also tested on  $\text{ZrO}_2\text{-MnO}$  and  $\text{Nb}_2\text{O}_5\text{-TiO}_2$  mixed oxide supports, which was reported to give even higher activities and selectivities.

Fan et al. [18] studied the effect of nickel promotion on lanthanum promoted

catalysts. 10% Co, 3% La on silica catalysts was promoted with up to 3% nickel. The nickel was shown to have a positive effect on the activity (with best effect at 1.5% loading), but no effect on selectivity. No information was given about how nickel was added to the catalyst. It was however observed that the cobalt and nickel particles did occupy the same spot on the support, while lanthanum did not.

Rytter et al. [3] did recently (2010) study the effect of nickel on alumina, silica and titania supports with or without rhenium promotion. They found that nickel had little effect on selectivity at alumina supports when the cobalt loading was higher than the nickel loading. At equal amounts of cobalt and nickel, selectivity toward heavy hydrocarbons was decreased. Nickel increases catalyst activity, but does also inhibit the effect of rhenium somewhat when both are present. The reduction temperatures for both reduction steps of cobalt were reduced by nickel promotion. This is claimed to be caused by hydrogen spillover. An in-situ XRD study where a 20% cobalt catalyst was compared with a catalyst promoted with 5% nickel was also carried out. The CoO intermediate particles was shown do decrease in size during the first reduction step. During the second reduction step, the particles seemed to sinter, and the metallic cobalt particles was shown to get approximately the same size as the  $\text{Co}_3\text{O}_4$  particles. This behaviour was equal for both catalysts, while a rhenium promoted catalyst was shown to inhibit the sintering in the second reduction step and thus increase dispersion. The nickel oxide particles were also shown to be small in size since they could not be detected with XRD. The nickel promoted catalysts were however shown to have a low initial activity during activity measurements, but increased in activity during the first hours on stream. They speculates whether this is caused by formation of alloys with low activity between nickel and cobalt during reduction. This alloy is assumed to separate into nickel and cobalt phases that is catalytically active during the first time on stream. The nickel promoted catalysts was also shown to have greater resistance to deactivation during the first 100 hours on stream, but was also shown to have greater sensitivity towards water.

Different methods of catalyst preparation were also evaluated by Rytter er al. [3]. A two step method where nickel was impregnated and calcined before cobalt was shown to give better activity than coimpregnated catalysts or catalysts where cobalt was added before nickel. They did also study nickel-support

interactions by calcinating a nickel on  $\gamma$ -alumina catalyst at high temperatures in order to make a spinel-like nickel aluminate on  $\alpha$ -alumina. Because of its high mechanical strength, further works by Rytter's group have focused on its use in attrition resistant catalysts [19, 20].

Due to its dependency toward the lanthanum promoter and low nickel loading, the work by Fan et al. is not comparable with the other two. The works by Ishihara et al. and Rytter et al. does both focus on different support materials. The fact that these works claims different nickel loadings to be the most effective towards activity and selectivity could possibly be caused by support interactions. In this project,  $\gamma$ -alumina is chosen as support material. It is then naturally to use loadings in the same range as Rytter et al. [3] and use the preparation method (calcination with nickel before cobalt) proved to give highest activities. Nickel promotion should be expected to increase reducibility since this is to a great extent demonstrated by the observations of decreased reduction temperatures by Rytter et al. [3]. The effect of nickel on dispersion is not as obvious, Ishihara et al. [14] did only observe small variations in particle sizes on silica supports. On the other hand, the observed increases in catalyst activity does not rule out the possibility as TOF is known to be independent of particle sizes in cobalt catalysts.

## 1.8 Catalyst preparation

The method of incipient wetness impregnation is a simple and widely used method of catalyst impregnation. An important concept for this method is the incipient wetness point of the support material, i. e. the amount of water that the support is able to absorb in its pore space without having free flowing liquid. The impregnation is carried out by dissolving a salt containing the wanted amount of metal in water (preferably deionized water in order to avoid contamination by ions of other metals). The total amount of solution should be identical to the wetness point of the support in order to avoid loss of metal that is not absorbed into the pores. The solution is then added to the support material before drying. The catalyst is dried in order to remove the water and deposit the metal in the form of ions at the catalyst surface [9, 21]. The heating rate during drying does however have a great influence on the catalyst structure: A too high value will deposit the ions at the outer surface and pore

mounts of the support as the solution is forced “out” by evaporation in the pores. However, a too low value will cause evaporation near the pore mouth first, and drive the ions toward the bottom of the pores as the air-water interface is retreating [21]. It is therefore important to use the same procedure for drying of all catalysts to secure conformity.

The catalysts are calcined after the drying in order to convert the deposited ions into metal oxide particles. During the calcination, the catalysts are heated in flowing air. Water and other volatile components are also driven off during the heating. The catalyst activity may be negatively influenced if the air stream falls too low. A stream of 16 ml air/min/g catalyst has been mentioned as a minimum value for Fischer-Tropsch catalysts before such effects kicks in [1].

## 1.9 Temperature programmed reduction

In order to make the catalysts active, the metal oxide particles must be converted into metal particles. Because the active catalysts become oxidized if exposed to oxygen, the catalysts are normally stored as metal oxides, and reduced in hydrogen or carbon monoxide in situ before use. The reduction of cobalt catalysts happens in two steps:



While nickel oxide is reduced in one step:



In the temperature programmed reduction (TPR) analysis, a sample of the catalyst is reduced in a flowing stream of diluted hydrogen at rising temperatures. The heating rate should be held constant, and the hydrogen consumption is measured by comparing the composition of the gas stream upstream and downstream to the sample. These measurements are usually done with thermal conductivity sensors. The reduction temperatures can be found as peaks in the hydrogen consumption, while the degree of reduction (the amount of metal oxide reduced) could be found by integration of the hydrogen consumption.

## 1.10 Thermal gravimetric/Differential thermal analysis

Like TPR, in thermal gravimetric analysis (TGA) and differential thermal analysis (DTA), properties are measured while the sample is heated. In TGA, weight changes in the sample is measured as the temperature is changing and the reaction temperature and extent of reactions that causes mass change can thus be examined. In DTA, the temperature of the sample is measured and compared with a blank sample that undergoes the same treatment. Variances in the measured heating rate can be used to identify endothermic or exothermic reactions. Equipment for TGA and DTA are often combined in the same unit while its exhaust may be measured with a mass or IR spectrometer in order to identify desorbed species or reaction products[22, 23].

## 1.11 Mass spectrometry

In mass spectrometry (MS), substances are identified by their molecular mass. Molecules are gasified and ionized before accelerated in an electric field. The ions are then identified by their mass-to-charge ratio by either measuring their speed (in a time of flight spectrometer) or by their deflection in a magnetic field (in a magnetic sector spectrometer) [24]. A third alternative is to use a quadrupole mass spectrometer where the mass-to-charge ratio is measured by studying the ion's movement through oscillating electrical fields [25]. The detected mass-to-charge ratios ( $\frac{m}{z}$ ) may represent a whole molecule (in this case,  $\frac{m}{z}$  is a quotient of the molecular mass and an integer charge:  $\frac{m}{z} = \frac{M_n}{1}, \frac{M_n}{2}, \dots$ ), or fragments of a bigger molecule.

## 1.12 X-ray diffraction

X-ray diffraction (XRD) is an analysis method that makes use of the fact that crystalline phases exposed to x-rays will yield a diffraction pattern that is typical for its structure. The intensity and angle of the diffracted radiation of x-rays sent upon a sample can be used to identify the structure of a crystalline

solid. Bragg's law describes how the diffraction angle ( $\theta$ , represented as diffraction peaks<sup>1</sup>) for x-rays with a given wave length ( $\lambda$ ) and the spacing between planes in the crystal structure ( $d_{hkl}$ ) are related [26]:

$$n\lambda = 2d_{hkl} \sin \theta \quad (1.12)$$

For a cubic crystal structure with Miller indices  $h$ ,  $k$  and  $l$ ,  $d_{hkl}$  can be calculated by:

$$d_{hkl} = \frac{a}{\sqrt{h^2 + k^2 + l^2}} \quad (1.13)$$

The placement of peaks in a x-ray diffractogram can thus be used to identify solid compounds present in a sample as these are unique for different compounds and phases. The shape of the peaks can also be used to measure the size of particles: Small particles will give wider diffraction peaks than big particles. This can be used to estimate particle size with the Scherrer equation [23]:

$$\langle L \rangle = \frac{K\lambda}{B \cos \theta} \quad (1.14)$$

Where  $B$  is the line broadening of a diffraction peak.  $B$  should be corrected from the observed peak width ( $B_{\text{obs}}$ ) by taking into consideration that the diffractometer also has it's own line broadening ( $B_{\text{inst}}$ ) [23]:

$$B^2 = B_{\text{obs}}^2 - B_{\text{inst}}^2 \quad (1.15)$$

$B_{\text{obs}}$  can be found by two different methods: Either by measuring the peak width at half the height between the baseline and the peak maximum, or by integrating the peak area divided by peak height. When using the half height peak width, the Scherrer constant,  $K$ , of 0.89 is normally used. For the integral method,  $K$  is usually set to 1 [9, 23]. Particle size must be calculated from the crystallite thickness,  $\langle L \rangle$ . Cobalt particles are usually assumed to be spherical, and a conversion factor of 4/3 is used to convert from crystallite thickness to particle diameters [1]. Upon reduction, the size of the metallic cobalt particles will usually be 3/4 of the size of the cobalt oxide particles [27]. The calculated values of  $\langle L \rangle$  for an unreduced catalyst should thus be representative for the particle size of a reduced one. This assumption is however somewhat inaccurate and the margin of error could be as high as 20-30% [28]. Cobalt is subject to

---

<sup>1</sup>Angles where x-rays are diffracted with higher intensity.

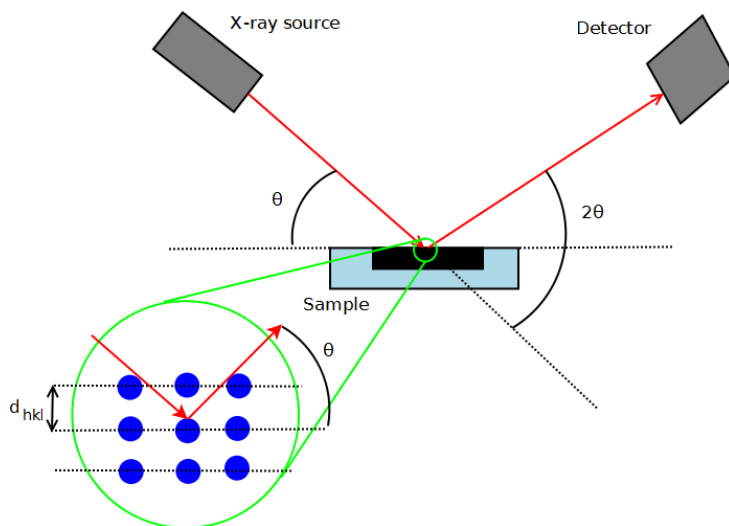


Figure 1.3: *Sketch of a powder XRD diffractometer.*

fluorescence when exposed to x-ray radiation from a copper source. Radiation emitted by cobalt will in these situation decrease the signal-to-noise ratio of the diffractogram. Increased sampling times or the use of a monochromator in a secondary position (in front of the detector) will increase the quality of the diffractograms. For a single crystal, the diffraction angles must be measured in three dimensions. For characterization of catalysts and other power samples, powder XRD is used. When a great number of small crystallites in the powder are randomly oriented in space, the characteristic diffraction peaks can be measured in a single plane through the sample thus simplifying the measurements. A simplified figure of a diffractometer is shown in figure 1.3.

## 1.13 Physisorption

Physisorption describes the bonding of gases to a solid surface by van der Waal forces. Typical for such bonding is that it has no activation energy and is thus easily reversible. Multiple layers of the adsorbed gas are also easily formed [29]. As physisorption has no selectivity towards different surfaces, it is suited to measure the total surface area (both metal particles and support) of a catalyst. The measurements are usually done by placing the catalyst samples in test

tubes and then evacuated in order to remove adsorbed gasses and moisture. The samples are then cooled down to a temperature close to the boiling point of the adsorbate and the dead volume is measured with a gas that adsorpes at a limited degree at the surface. The adsorbate is then added to the test tubes at different pressures and physisorped volumes are measured and found by comparison with the dead volume [21].

Monolayer formation is normally assumed to follow the Langmuir isotherm when the ratio between the pressure and the saturation pressure ( $p/p_0$ ) is lower than 0.1. At higher pressures, multilayer formation kicks in and are assumed to follow the Brunauer, Emmet and Teller (BET) isotherm when  $p/p_0 \leq 0.3$  [21, 30]:

$$\frac{p}{V_{ads}(p_0 - p)} = \frac{C - 1}{V_{ML}C} \frac{p}{p_0} + \frac{1}{V_{ML}C} \quad (1.16)$$

Equation 1.16 shows a linear relation between  $\frac{p}{V_{ads}(p_0 - p)}$  and  $\frac{p}{p_0}$ . By plotting these values against each other, the slope ( $\frac{C-1}{V_{ML}C}$ ) and intercept at zero pressure ( $\frac{1}{V_{ML}C}$ ) are found by regression. The monolayer coverage,  $V_{ML}$  are then easily found. The surface area is then calculated using equation 1.17 [21, 29]:

$$A_S = \frac{V_{ML}aN_A}{V_m} \quad (1.17)$$

## 1.14 Chemisorption

By measuring the chemisorption of a reduced catalyst, the metal surface available for adsorption can be determined. The chemisorption measurement is done by measuring the gas volume adsorbed by the sample at different pressures. The gas chosen for this measurement must be able to chemisorb at the actual metal. The gas also undergoes physisorption on the support material and the measurements must be corrected for this effect. Ideally, it can be assumed that the chemisorption are following the Langmuir isotherm and that the physisorption is proportional with the pressure. The measured adsorption isotherm is then the sum of the Langmuir isotherm and the physisorption isotherm. The gas volume needed to cover the metal surface (monolayer coverage) can then be found by linear interpolation of the measured isotherm towards zero pressure. An alternative method is to evacuate the sample and measure a second adsorption isotherm. It is assumed that the physisorped gas

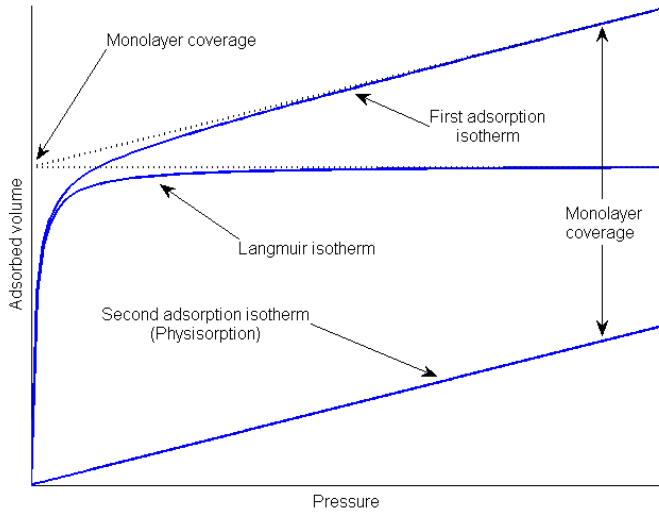


Figure 1.4: *Isotherms used in chemisorption measurements.*

is desorbed during the evacuation while the chemisorbed gas is strongly bound to the surface and do not desorb. This adsorption isotherm is assumed to only describe physisorption since the sites available for chemisorption are already occupied. The monolayer coverage can then be found by subtraction of the isotherms with each other [30]. See figure 1.4 for a graphical representation of this model. It should be noted that this the two methods of calculation could give different results caused by factors like desorption of weakly bound chemisorbed gas during evacuation.

When the gas volume at monolayer coverage is found, the dispersion (the ratio between metal available for chemisorption and total metal loading) can then be calculated with the following equation [8]:

$$D = \frac{V_{ads}M_n\nu}{w_m} \quad (1.18)$$

Where  $\nu$  is the stoichiometric coefficient of adsorption,  $w_m$  is the metal loading and  $V_{ads}$  the adsorbed volume. The mean particle size can be estimated by dividing a shape factor with the dispersion. The shape factor depends on both the particle shape and density of sites available for chemisorption on the particle

surface. Assuming a spherical cobalt particle, a factor of 96 could be used [1]:

$$d = \frac{96}{D} \quad (1.19)$$

In order to distinguish between different metals in a bimetallic catalyst by chemisorption, measurements with different gasses where the metals shows different adsorption stoichiometry or don't chemisorb at all is necessary [31].

## Chapter 2

# Experimental work

The experimental work of this thesis are carried out with two purposes: 1) To investigate how nickel promotion influences reducibility, and: 2) To investigate how nickel promotion influences metal dispersion. Temperature programmed reduction was chosen to measure reducibility because of its simplicity in both operation and data analysis. Dispersion was measured by chemisorption since this method is able to measure the wanted property in a direct way. Both in- and ex-situ XRD were used to measure particle sizes prior to- and after reduction. As particle size is a property closely related to dispersion, XRD should give useful information about both dispersion and reducibility (through in-situ analysis).

The experimental work was carried out in accordance with established practice in the catalysis group at NTNU and methodology in other relevant works about the Fischer-Tropsch synthesis such as [1] and [3]. All experimental work was carried out at NTNU Gløshaugen, using equipment owned by the Department of Chemical Engineering, the Department of Materials Science and Engineering and SINTEF Materials and Chemistry.

### 2.1 Catalyst preparation

The catalysts studied in this work were all made by impregnation by the incipient wetness method followed by calcination. The bimetallic catalysts were

either coimpregnated with multiple metals at once, or underwent this treatment twice so the second metal was added to a calcined catalyst with the first metal. A  $\gamma$ -alumina provided by SASOL (PURALOX SCCa Z500200 developmental product) with a pore volume of 720 ml/g and a surface area of 150 m<sup>2</sup>/g was used as support material for the catalysts. The method of incipient wetness was chosen because of its simplicity and comparability with other works.

Cobalt nitrate hexahydrate ( $\text{Co}(\text{NO}_3)_2 \cdot 6\text{H}_2\text{O}$ ) supplied by Acros organics (99+% purity) and nickel nitrate hexahydrate ( $\text{Ni}(\text{NO}_3)_2 \cdot 6\text{H}_2\text{O}$ ) supplied by Sigma-Aldrich (99.999% purity) were used as precursor salts for the catalysts. The salts were soluted in deionized water and poured into a rotating bowl containing the support material in order to achieve a uniform distribution. The support had a wetness point of 1.3273 grams of water per gram of support. The amount of crystal water in the salts was calculated and subtracted from this number in order to find the correct amount of solvent. After the first impregnation and calcination, the wetness point seemed to decrease somewhat. An exact wetness point for the catalysts was not measured at this point since it was assumed to vary with the metal content, and an approximation of 0.5 grams of water per gram of catalyst without any correction of the content of crystal water was used instead. The support was not dried prior to the impregnation. The impregnated catalysts were dried for 3 hours at 103 °C while stirred each 15 minutes.

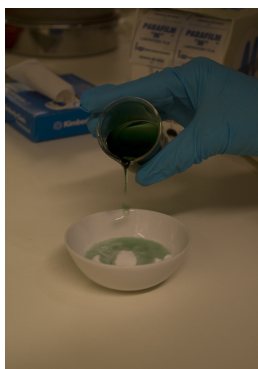


Figure 2.1: *Impregnation of catalyst.*

A series of catalysts were made with loadings of 20% Co and 1, 5 or 10% Ni produced in two steps, where nickel was impregnated and calcined during the first step. Since Rytter et al. [3] found catalysts prepared in this order to be more active, this thesis will focus at these catalysts. Some catalysts with high nickel loadings (5 and 10%) were made for comparison by coimpregnation or with addition of cobalt before nickel in a two step synthesis. The reason for making the 10% nickel catalysts with higher loadings than described in literature, is to increase the observability when using XRD.

Two additional catalysts (one with 20% Co and one coimpregnated with 11% Co, 5% Ni) were made to test an alternative method of impregnation where

the catalysts were dried under vacuum. The support was placed in a modified round-bottom flask and stirred with a magnetic stirrer, while the metal salt solution was injected with a syringe. The flask was then evacuated with a vacuum pump and placed in an oil bath that held a temperature of  $\sim 90$  °C. The catalyst was then dried in this set up for 28 hours. The set up used is shown in figure 2.2.

These two catalysts were made and tested as a side project together with my supervisor. The aim for this project was to test the effect of drying under vacuum on catalyst dispersion and these catalysts were not used in connection with the rest of the thesis work.

The calcination was done in a fixed bed glass reactor in flowing air (22 ml/min/g catalyst) at ambient pressure. The catalysts were heated at a rate of 2 °C/min up to 300 °C and held at this temperature for 16 hours. While a bit high when compared with other works [1], an air stream of this size was chosen to reduce the consequences of small leaks in the calcination set up.

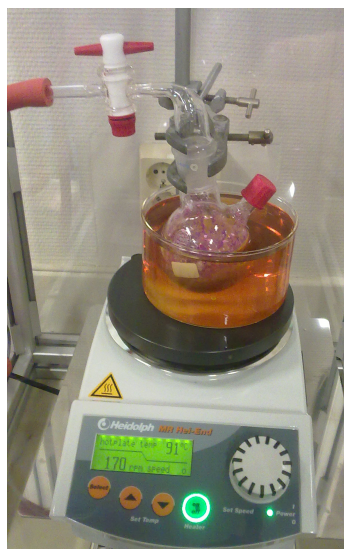


Figure 2.2: Set up for drying of catalysts under vacuum.

## 2.2 Temperature programmed reduction

Temperature programmed reduction (TPR) measurements were carried out using a Quantachrome CHEMBET-3000 apparatus (figure 2.3). Samples with a size of 0.100 grams were placed between quartz wool plugs in a U-formed glass reactor. The reactor was connected to the apparatus and placed inside a furnace. The catalyst was reduced by a flowing gas stream containing 7% hydrogen diluted in argon and heated at a rate of 10 °C/min up to a temperature of 820 °C. A gas stream of 50 ml/g<sub>catalyst</sub>/min was used, while some catalysts were also studied with gas streams in the range of 190-200 ml/g<sub>catalyst</sub>/min. Hydrogen consumption was measured with a thermal conductivity sensors at a sampling rate of 5 s<sup>-1</sup> and logged with the TPRWin software, while data

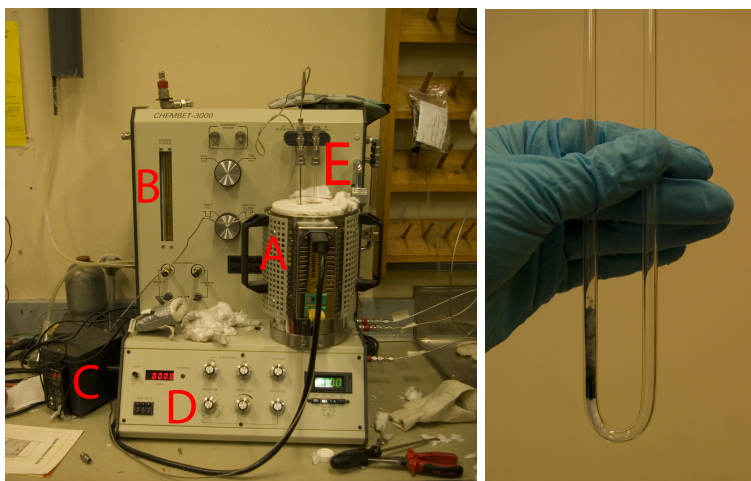


Figure 2.3: Left: CHEMBET-3000. A: Furnace. B: Flowmeter. C: Temperature controller. D: Control panel. E: Reactor. Right: Reactor with sample.

analysis were carried out using MATLAB.

## 2.3 TGA/DTA/MS

The TGA and DTA analysis were carried out using a Netzsch STA 449 C TG-DTA/DSC unit connected to a MS 403 C Aëolos quadrupole mass spectrometer (figure 2.4). Samples with a size of 50 mg was placed in a sample holder at a microbalance. The sample holder was connected to a thermocouple used for the DTA analysis. An empty sample holder was connected to another thermocouple and placed next to the used sample holder as a reference. The samples and microbalance was then enclosed in a reaction chamber with an outlet to the mass spectrometer. The catalysts were then reduced in a gas stream of 12 %  $H_2$  diluted in argon flowing at 50 ml/min while heating to 900 °C at a rate of 10 °C/min. The Netzsch Measurement 4.8.4 software was used for data logging and control, while the Netzsch Proteus thermal analysis 4.8.4 and Inficon display saved values 7.0.2 software were used for analysis. Blank runs were done before each analysis in order to make correction files for the analysis software.



Figure 2.4: *Left: TGA/DTA set-up. A: Mass spectrometer. B: Furnace. C: Microbalance. D: Instrument and temperature controls. Right: Sample holder with sample and empty sample holder used as reference at top of the microbalance.*

## 2.4 Physisorption

Physisorption was measured in a Micromeritics TriStar 3000 device (figure 2.5).

Samples were placed in test tubes and evacuated overnight at 150 °C. Dead volume was measured with helium, while adsorption isotherms were measured using nitrogen as an adsorbate. The adsorbed volume was measured at five different pressures in the range 50 - 150 torr. while the samples was cooled with liquid nitrogen at -196 °C during the measurements. The TriStar 3000 6.05 software was used for data logging, control and analysis.



Figure 2.5: *Micromeritics TriStar 3000. A: Test tubes with samples. B: Raisable flask with liquid nitrogen.*

## 2.5 Chemisorption

Chemisorption measurements were carried out with a Micromeritics ASAP 2020 device (figure 2.6). Samples in the range of 0.3-0.4 grams of catalyst were placed between quartz wool plugs

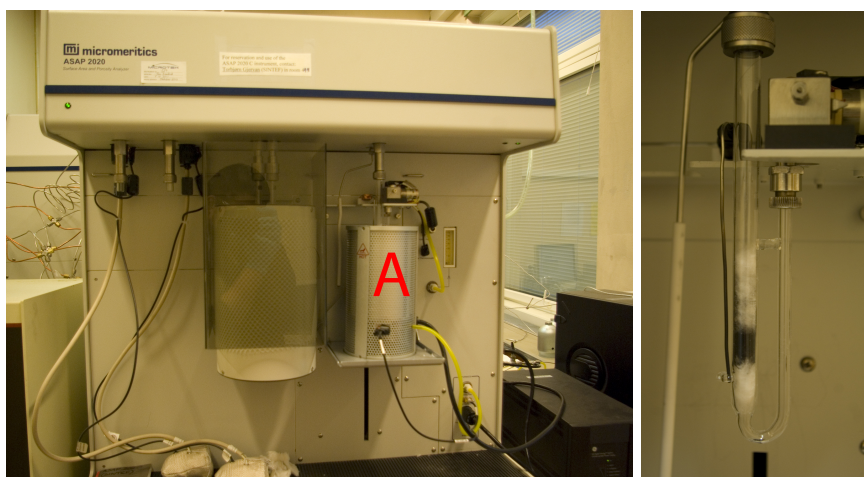


Figure 2.6: *Left: Micromeritics ASAP 2020. A: Furnace covering the reactor. Right: Reactor with sample.*

in a U-formed glass reactor that was placed in a furnace. Prior to the measurements, the sample was reduced in flowing hydrogen at ambient pressure while heating at a rate of  $1\text{ }^{\circ}\text{C}/\text{min}$  up to  $350\text{ }^{\circ}\text{C}$  and held at that temperature for 10 hours. The sample was evacuated both prior to and after cooling down at a rate of  $10\text{ }^{\circ}\text{C}/\text{min}$ . A leak test was carried out before the measurements. Chemisorption of hydrogen was measured with 10 points of measurement at pressures in the range of 15 - 500 torr at a constant temperature ( $40\text{ }^{\circ}\text{C}$ ). The ASAP 2020C software was used for data logging, control and analysis.

## 2.6 X-ray diffraction

Powder X-ray diffraction (XRD) analysis was carried out both ex-situ on calcined catalysts and in-situ during catalyst reduction. The ex-situ analysis was carried out with a Siemens D5005 diffractometer (figure 2.7). The diffractometer was equipped with a copper X-ray source, a scintillation detector and a secondary graphite monochromator. Diffractograms were taken overnight with values of  $2\theta$  in the range of  $5^{\circ}$ - $100^{\circ}$ , step size of  $0.01^{\circ}$  and a measurement time of 5.7 seconds per step.

The in-situ analysis were carried out in a Bruker D8 advance diffractometer equipped with a copper X-ray source (figure 2.7). A scintillator detector

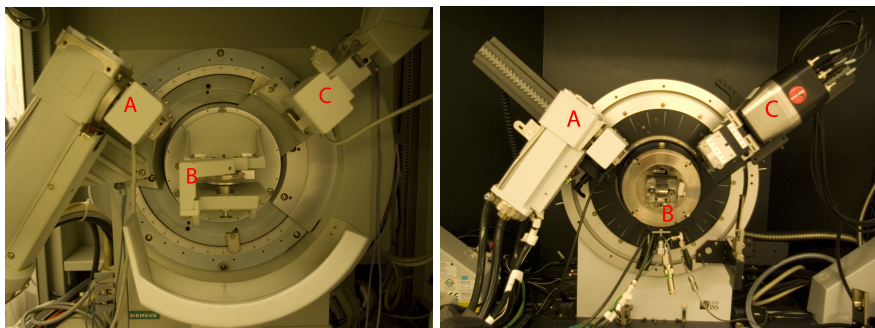


Figure 2.7: *Siemens D5005 diffractometer (left) and Bruker D8 advance (right). A: X-ray source. B: Sample holder (in opened reaction chamber for D8 advance). C: Detector.*

equipped with a secondary monochromator was used with the cobalt containing samples, while a fast-scanning Vântec detector was used for the other samples. The sample was placed in a reaction chamber from MRI Physikalische Geräte.

The in-situ analysis were carried out on a few selected samples. The samples were reduced at ambient pressure, and in an atmosphere of 7% hydrogen diluted in nitrogen flowing through the reaction chamber. The reaction chamber was also flushed with nitrogen and leak tested before the measurements. Two different reduction programs were used: One where the sample was heated to 350 °C at a rate of 3 °C/min and held at that temperature for 16 hours before cooling down to 30 °C at a rate of 10 °C/min. Four diffractograms were taken at 350 °C with a range of  $2\theta$  of 15°-75°, a step size of 0.03° and a measurement time of 7.2 seconds per step. Another diffractogram was taken at 30 °C after cooling down with the same range and step size, but a measurement time of 12 seconds per step.

Another analysis was carried out where the samples was heated to 900 °C with a rate of 10 °C/min. The heating was stopped every 50 °C between 150 °C and 900 °C in order to take a diffractogram. Diffractograms were also taken before the heating started and after cooling to 30 °C. The range and speed of measurement varied with the nature of the samples and temperature, and is shown in table 2.1. The temperature programs of the in-situ analysis are illustrated in figure 2.8.

The XRDcommander software was used for logging and control of both diffractometers, while Bruker AXS EVA 2 and Topas 4.2 were used for data analysis.

Table 2.1: Parameters used in in-situ XRD while heating to 900 °C.

	Detector	$2\theta$ -range	Step size	Measurement time [s/step]
With Co, before heating	Scintillator w/ monochromator	15°-75°	0.03°	7.2
With Co, 150-700 °C	Scintillator w/ monochromator	23°-72°	0.03°	8
With Co, 750-900 °C	Scintillator w/ monochromator	23°-72°	0.02°	8
With Co, after cooling	Scintillator w/ monochromator	15°-75°	0.02°	14.4
Without Co	Väntec	15°-72°	0.0245°	1.2

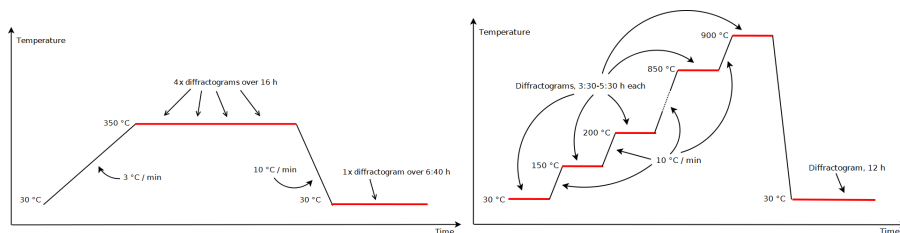


Figure 2.8: *Temperature programs of in-situ XRD analysis. Left: Reduction at 350 °C for 16 h. Right: Reduction of Co-catalysts while heating to 900 °C.*

## 2.7 Risk assessment

A risk assessment was carried out before the start of the experimental work. An updated version of the risk assessment can be found in appendix D.

# Chapter 3

## Results and discussion

The results of the experimental work are presented in this chapter. Section 3.1 to 3.6 presents the measurements of the catalysts that was made in two steps with nickel first. Measurements of catalysts prepared in other ways are presented and discussed in section 3.7. Trends observed about reducibility and dispersion are discussed in sections 3.8 and 3.9. Additional measurements and data that did not fit naturally into the discussions in this chapter, can be found in appendix C, while appendix B contains examples of calculations carried out during the data analysis.

### 3.1 Physisorption

The support and various unreduced catalysts had their physisorption measured, and surface areas calculated by the BET-method. These surface areas are shown in table 3.1. It is shown that the surface area decreases when the support is loaded with cobalt or nickel, and then to increase even more when the catalyst is impregnated and calcinated a second time. The surface area of catalysts that were impregnated and calcinated a second time did not vary for different nickel loadings.

Table 3.1: Surface areas measured by physisorption

Composition	Surface area [ $m^2/g$ ]
Support	154
6,3 % Ni	136
20% Co	120
20% Co, 1% Ni	107
20% Co, 5% Ni	109
20% Co, 10% Ni	106

### 3.2 Ex-situ XRD

The diffractograms obtained of the support and the unreduced catalysts were inspected visually in order to find the characteristic diffraction peaks. The peaks found were compared with peaks of the same compounds in the powder diffraction database in the software and found to be in accordance. Diffractograms of the support and a catalyst loaded with cobalt oxide are shown in figure 3.1, while catalysts loaded with nickel only are shown in figure 3.2. Since both cobalt oxide, nickel oxide and  $\gamma$ -alumina have cubic structures, the placement of their peaks are only differing with the variations of their lattice parameters. The peaks are therefore seen to be placed close to each other or overlapping. The nickel oxide peaks are not visible in the 6.3% Ni catalyst, and the peaks shown for the 10% Ni catalyst are barely visible. This should be seen as an indication of that the size of the nickel oxide particles close to what is observable with XRD, and that the nickel oxide thus is of higher dispersion than the cobalt oxide. Nickel oxide peaks was not observed in any of the Ni-promoted cobalt catalysts, probably due to overlap between the cobalt oxide and nickel oxide peaks.

The particle sizes were then calculated with the Scherrer equation using the TOPAS software. The software treats the diffractogram as a superposition of different peaks and fits the measured data numerically to peaks calculated from the lattice parameters and crystal structure of the different phases. The  $\gamma$ -alumina support did however fit poorly to the peaks calculated by the software. The support was instead modelled with an alternative approach: Diffractograms of the support was fitted to a model of multiple independent peaks.

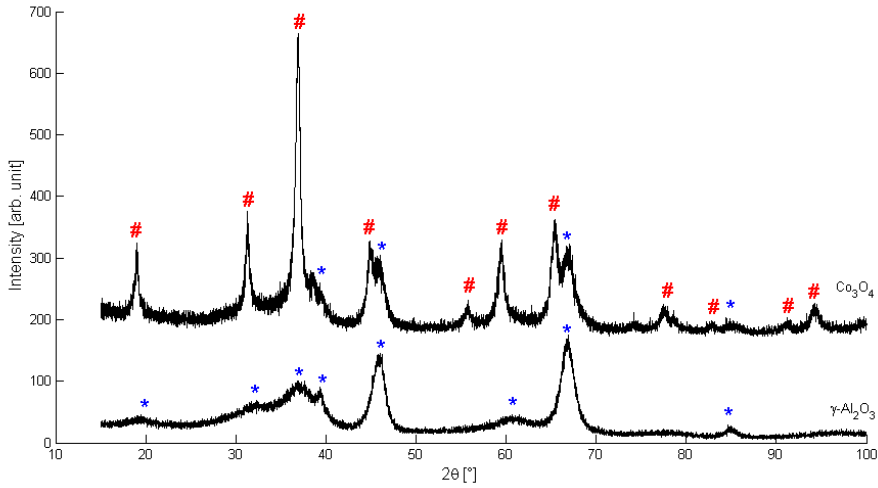


Figure 3.1: *Diffractograms of support (bottom) and an unreduced catalyst loaded with 20% Co (top). Visible peaks for  $\text{Co}_3\text{O}_4$  (#) and  $\gamma\text{-Al}_2\text{O}_3$  (\*) are marked. Notice how the cobalt oxide and alumina peaks are overlapping.*

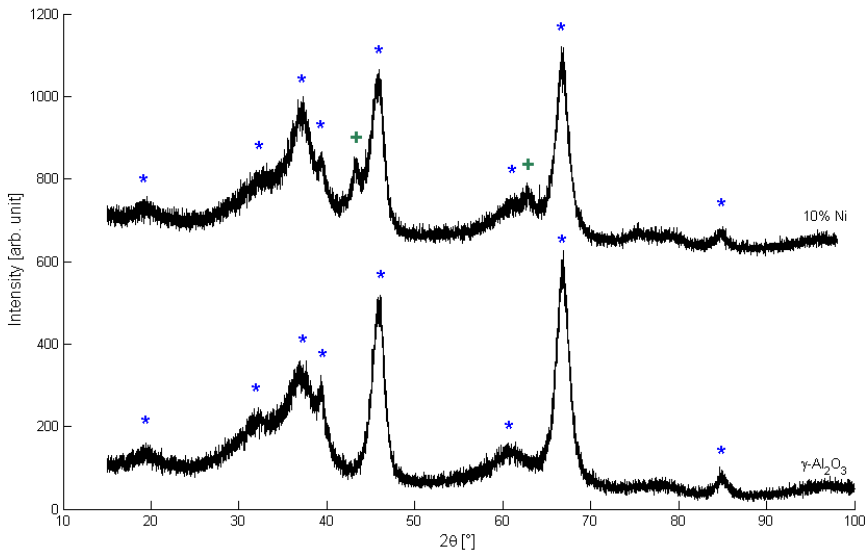


Figure 3.2: *Diffractograms of support (bottom), and unreduced catalyst with 10% Ni loading (top). Visible peaks for NiO (+) and  $\gamma\text{-Al}_2\text{O}_3$  (\*) are marked. The height of the peak at  $2\theta = 37^\circ$  is increased for the 10% Ni-catalyst, which indicates an additional NiO-peak at this position overlapping with the  $\gamma\text{-Al}_2\text{O}_3$ -peak.*

Table 3.2: Particle sizes of  $\text{Co}_3\text{O}_4$  calculated from XRD

	Calculated crystallite size, $\langle L \rangle$ [nm]	Estimated particle size, $d$ [nm]
20% Co	13.7	18.2
20% Co, 1% Ni	13.8	18.5
20% Co, 5% Ni	13.1	17.5
20% Co, 10% Ni	12.6	16.9
10% Ni	3.6	4.8

This model was then linked to the diffractograms of the catalysts and the two diffractograms were solved simultaneously. This method is described further details in appendix A. Crystallite sizes calculated with the half height peak broadening method are used for every diffractogram in this thesis as described further in the next section. The Scherrer constant ( $K$ ) was set to 0.89 in all calculations. The calculated values are shown in table 3.2 as both crystallite sizes and particle sizes assuming spherical particles.

### 3.3 In-situ XRD

A catalyst with 20% Co only, and a catalyst loaded with 20% Co, 10% Ni were reduced at 350 °C for 16 hours. The diffractograms obtained during and after the reduction were investigated and the peaks were identified using the powder diffraction database. A diffractogram of the reduced 20% cobalt catalyst is shown in figure 3.3. The fcc cobalt phase was the only visible metallic phase in both the 20% Co and the 20% Co, 10% Ni catalysts. Since both the metallic cobalt and nickel are of fcc structures, their peaks are expected to overlap. Formation of a cobal-nickel alloy is also possible. Principally, alloy formation should be detectable with XRD as changing peak positions due to changed lattice parameters [15]. In this case, the expected change in peak positions for the [1,1,1]-peak was calculated to 0.1°, which is too narrow for detection. Cobalt oxide (CoO) peaks were barely visible in both catalysts after reduction for 4 hours, and completely gone after 8 hours. This is shown in figure 3.4 where diffractograms of the 20% Co, 10% Ni catalyst is compared after 4 and 16 hours of reduction. The particle sizes of the metal particles were calculated with the Scherrer equation using TOPAS. Particle sizes of the reduced catalysts was

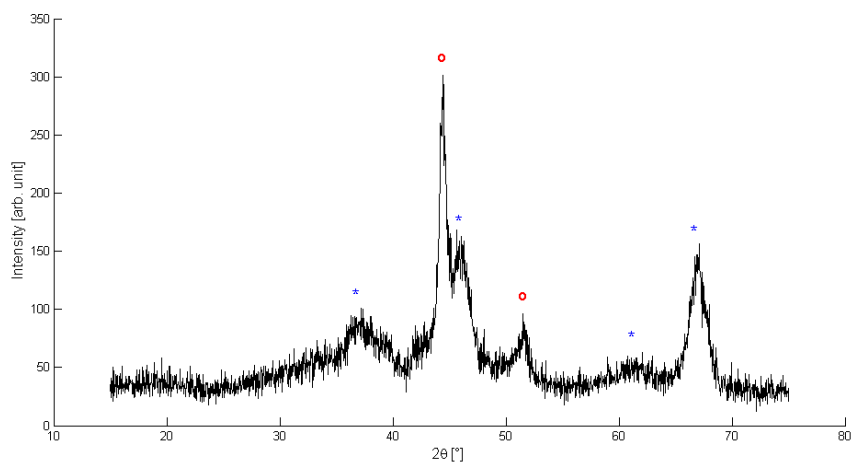


Figure 3.3: Catalyst loaded with 20% Co after reduction for 16 h at 350 °C. Visible peaks for fcc-Co (o) and  $\gamma$ - $\text{Al}_2\text{O}_3$  (\*) are marked.

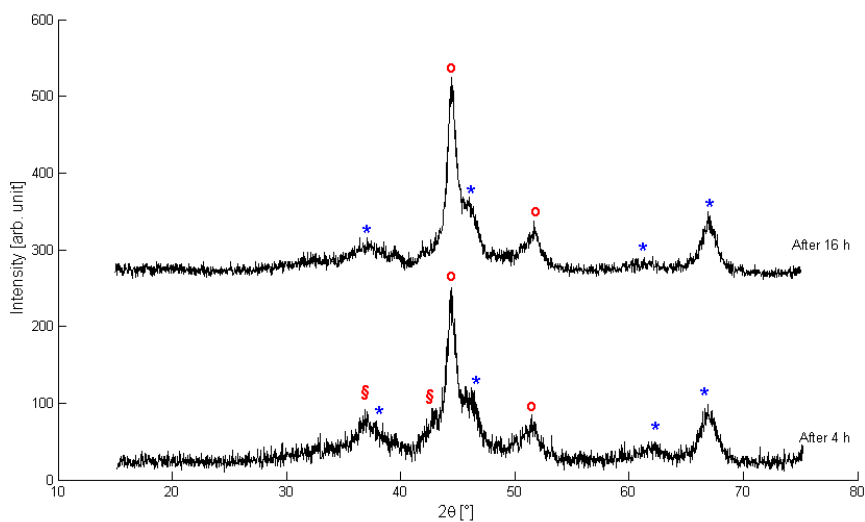


Figure 3.4: Catalyst loaded with 20% Co, 10% Ni after reduction for 16 h at 350 °C. Visible peaks for fcc-Co (o), CoO (§) and  $\gamma$ - $\text{Al}_2\text{O}_3$  (\*) are marked.

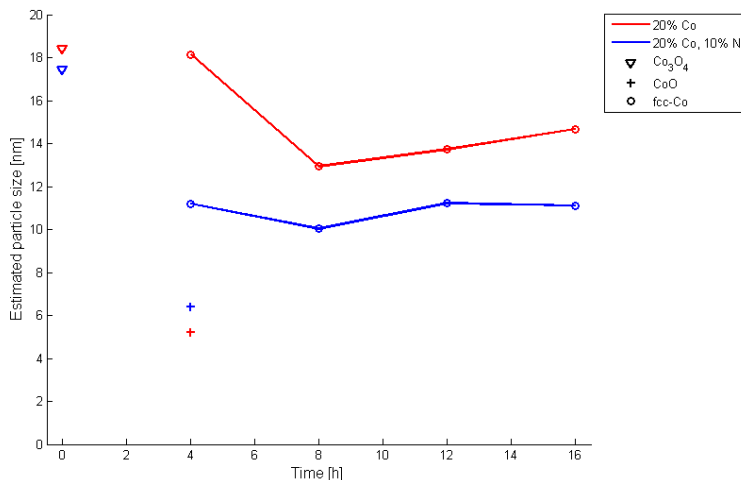


Figure 3.5: *Development of the 20% Co catalyst (red) and the 20% Co, 10% Ni catalyst (blue) during reduction. Observe that the figure is not taking the heating time into account. The size of the metallic cobalt particle after 4 hours in the 20% Co catalyst is probably overestimated due to overlap with the CoO particle.*

calculated with both the half height peak broadening and the integral height method. Spherical particles was assumed in both cases. When compared with the chemisorption results (see section 3.6), particle sizes calculated with the half height peak broadening method was shown to be more in accordance. This method was then chosen to calculate all diffractograms in this thesis. The calculated values in means of particle diameter are shown in figure 3.5. It is shown little development in the cobalt particle sizes after the first four hours of reduction. Cobalt particle sizes are however shown to be 25% smaller in the nickel containing catalyst than in the catalyst containing cobalt only, indicating a higher dispersion in the nickel promoted catalyst.

A 20% Co catalyst, a 10% Ni catalyst, a 20% Co catalyst promoted with 10% nickel heated to 900 °C under reduction conditions. A sample of support was also analysed with the same program for comparison. Diffractograms of the 20% Co catalyst taken during the heating are shown in figure 3.6, while diffractograms of the 20% Co, 10% Ni catalyst are shown in figure 3.7. Diffractograms of the nickel catalyst and the support are not shown here, but can be found in

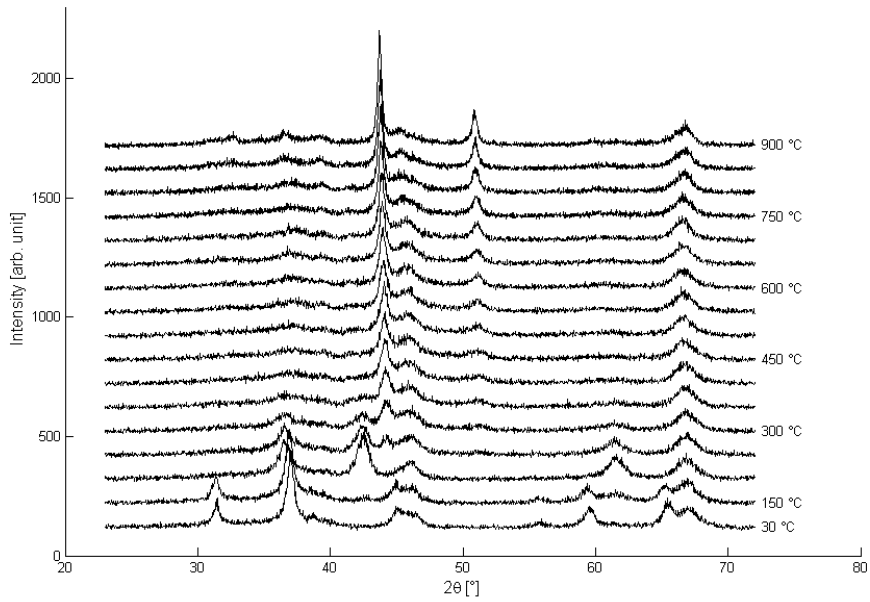


Figure 3.6: *In-situ XRD of a 20% Co catalyst heated to 900 °C.*

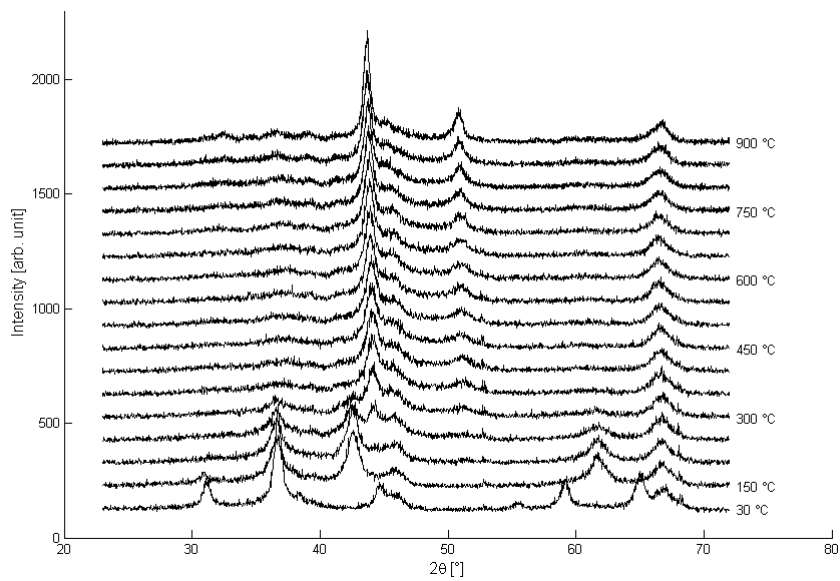


Figure 3.7: *In-situ XRD of a 20% Co, 10% Ni catalyst heated to 900 °C.*

appendix C p. 69. The  $\text{Co}_3\text{O}_4$  and fcc-Co peaks are already identified, while the peaks shown at  $2\theta = 42.6^\circ$  and  $61.8^\circ$  in these diffractograms were identified as CoO. By comparison of figures 3.6 and 3.7, one can clearly see that reduction to CoO starts beneath  $150^\circ\text{C}$  in the nickel-containing catalyst and between  $150$  and  $200^\circ\text{C}$  in the catalyst containing only cobalt. Reduction of CoO towards metallic cobalt is shown to start between  $200$  and  $250^\circ\text{C}$  in both catalysts. This indicates that promotion with nickel increases the reducibility of the first reduction step. The main cobalt peak is shown to sharpen at elevated temperatures in both catalysts, indicating sintering. The only change in the  $\gamma$ -alumina support shown during heating was the growth of a peak near  $2\theta = 32.6^\circ$  at temperatures above  $700^\circ\text{C}$ . Literature [32] describes  $\delta$ -alumina formation around these temperatures, which should be shown as a peak near the observed position. This peak is shown in detail at p. C.3. A sample of  $\gamma$ -alumina that was heated to  $900^\circ\text{C}$  at a rate of  $1^\circ\text{C}/\text{min}$  was seen to lose 60% of its surface area when measured with physisorption.

Before particle sizes could be estimated from the diffractograms, changes in the lattice parameters due to thermal expansion had to be accounted for. Lattice parameters were calculated from the measured peak positions at elevated temperatures and fitted to the following functions:

$$a_{fcc-\text{Co}}[nm](T[K]) = -9.185 \cdot 10^{-13}T^3 + 7.273 \cdot 10^{-9}T^2 - 3.562 \cdot 10^{-6}T + 0.3549 \quad (3.1)$$

$$a_{fcc-\text{Ni}}[nm](T[K]) = -1.044 \cdot 10^{-11}T^3 + 2.651 \cdot 10^{-8}T^2 - 1.343 \cdot 10^{-5}T + 0.3526 \quad (3.2)$$

These functions are valid in the range  $400 - 900^\circ\text{C}$ . The calculated particle sizes are shown in figure 3.8. The CoO particles are here shown to be smaller in size than both the  $\text{Co}_3\text{O}_4$  and the metallic cobalt particles. This is in accordance with observations by Rytter et. al. [3]. Whether this change is caused by cobalt oxide particles splitting up during the first reduction step, or by areas of amorphous CoO can not be determined from these data. The particles in the cobalt only catalyst seems to sinter together during the second reduction step. After the second reduction step, the size of the metallic cobalt particles are close to  $3/4$  of the cobalt oxide particles, which is typical for cobalt particles. The nickel promoted catalyst shows few signs of sintering during the second reduction step. In the 20% Co catalyst, the particle sizes at  $450^\circ\text{C}$  are 80% of the  $\text{Co}_3\text{O}_4$  particles at  $30^\circ\text{C}$  and 140% of the CoO particles at  $200^\circ\text{C}$ . In the

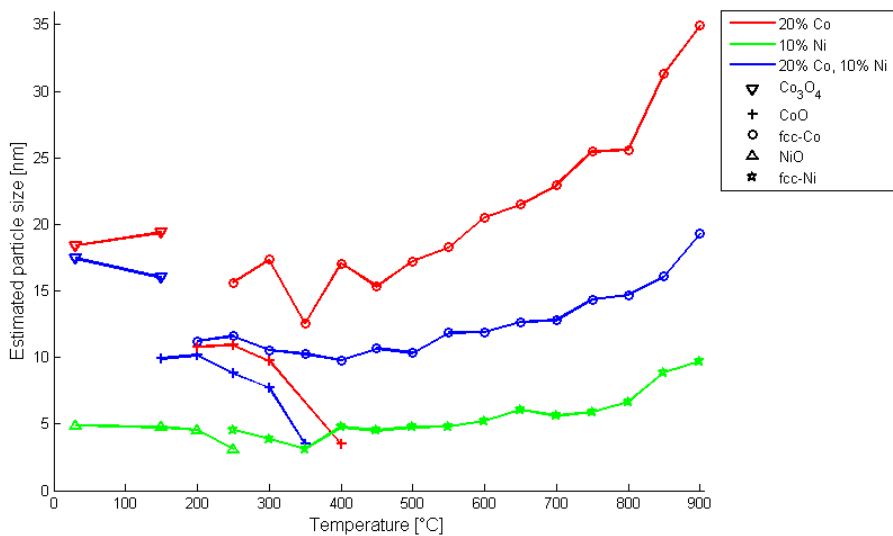


Figure 3.8: *Development of particle sizes during heating to 900 °C under reduction conditions. Observe that the variations in the Co particles of the 20% Co catalyst in the range 250-400 °C are probably caused by erroneous peak fitting by the TOPAS software and should not be interpreted as variations in the physical particle size.*

nickel-containing catalyst, the metal particles are of a size of 60% of the  $\text{Co}_3\text{O}_4$  particles at 30°C and 105% of the CoO particles at 200 °C. Between 450 and 900 °C, the size of the cobalt particles of the 20% Co catalyst increases with 130%, while the particles in the nickel containing catalyst increases with 80%. These observations indicate that nickel counteracts the sintering during the second reduction step and thus promotes greater dispersion. Nickel promotion also seems to inhibit sintering at elevated temperatures. It should be noted that this contradicts the observations made by Rytter et. al. [3] of a 20% Co, 5% Ni catalyst. The particles in the 10% Ni catalyst shows no change in size during reduction. The nickel particles do increase in size by 120% between 450 and 900 °C, this is not directly comparable with the sintering of the cobalt catalysts due to the difference in time scale between the experiments (65.4 hours for the cobalt containing catalysts versus 12.4 hours for the nickel catalyst).

### 3.4 TPR

TPR profiles of a 20% Co catalyst and a catalyst precursor loaded with 6.3%  $\text{Ni}^1$  are shown in figure 3.9. The cobalt catalyst is shown to have a small peak near 250 °C, a sharp peak near 365 °C and a wider peak near 600 °C. In the literature [33], the first peak is identified as residual nitrates that are left in the pore structure after the calcination. The second peak close to 365 °C is caused by the first reduction step of cobalt oxide (reaction 1.9), while the last broad peak is the final reduction step to metallic cobalt (reaction 1.10). The nickel oxide is seen to be reduced to metallic nickel in one step at 340 °C (reaction 1.11). As nickel seems to be reduced at a somewhat lower temperature than cobalt, it is possible that the reduced nickel could promote the reduction of cobalt by hydrogen spillover.

Comparison of catalysts with a loading of 20% Co and 0-10% Ni are shown in figure 3.10. The peak representing the first reduction step is shown to be similar for catalysts loaded with 0 or 1% nickel (around 370 °C) and catalysts loaded with 5 or 10% nickel (around 330 °C). However, the wide peak representing the second reduction step did not seem to change. A standard error for the placement of peak representing the first reduction step was estimated to 16

---

<sup>1</sup>A sample taken aside after the first calcination while making a 20% Co, 5% Ni catalyst, not a precursor as in precursor salts.

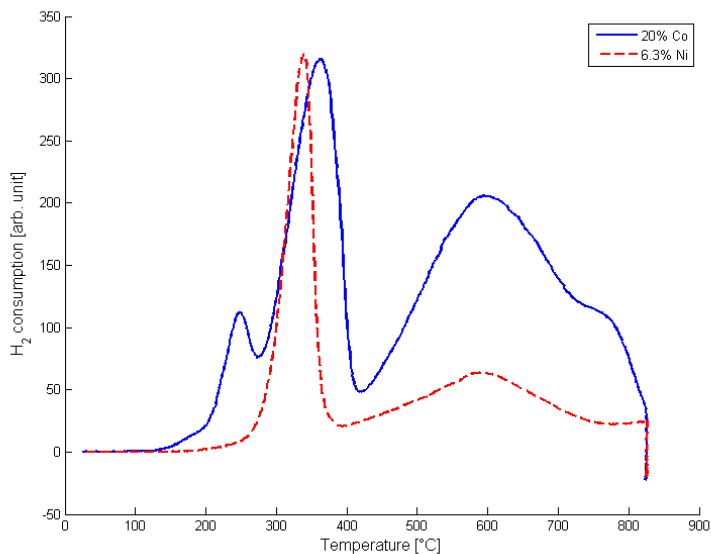


Figure 3.9: Comparison of TPR-profiles of a 20% Co catalyst (blue line) and a 6.3% Ni catalyst (red dotted line)

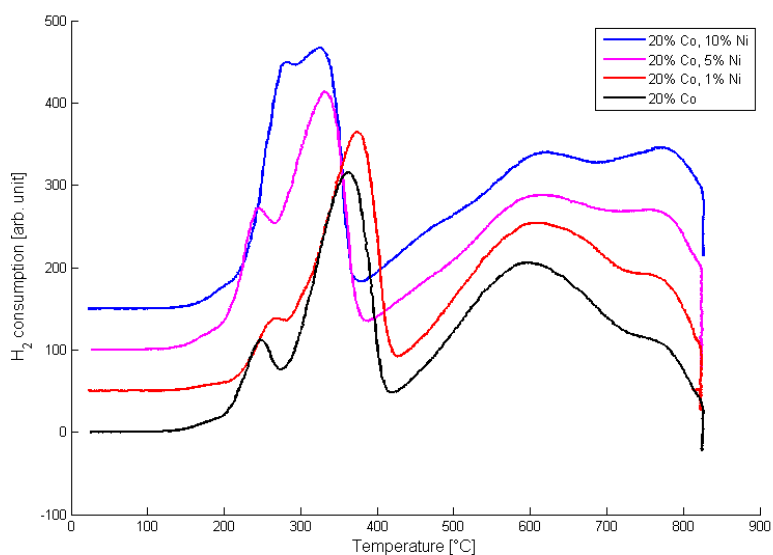


Figure 3.10: Comparison of TPR-profiles for catalysts with loading 20% Co, 0-10% Ni.

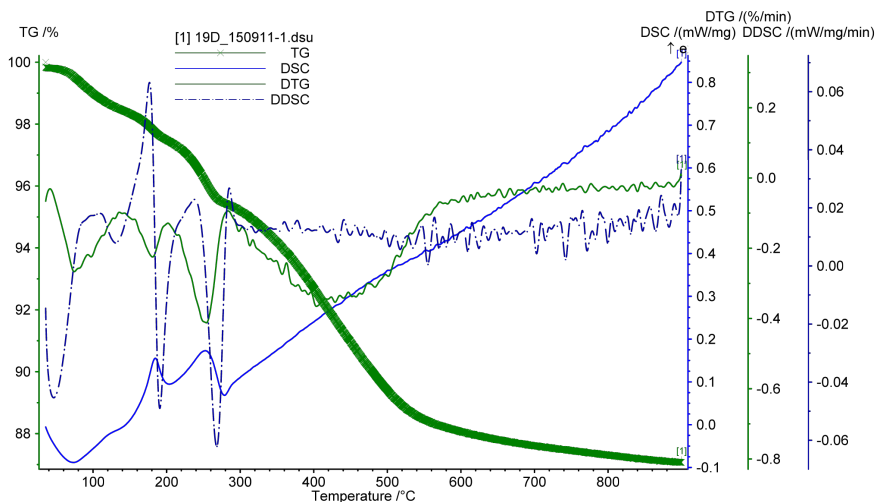


Figure 3.11: TGA (thick green) and DTA (blue) curves of a 20% Co, 5% Ni catalyst during reduction plotted together with their derivatives (thin green and dotted blue line).

°C. Some catalysts were also tested at higher flow rates (200 ml/g<sub>catalyst</sub>/min instead of 50 ml/g<sub>catalyst</sub>/min). The placement of the reduction peaks was here shown to decrease with around 50 °C, and gave a sharper peak representing the second reduction step. The difference in observed reduction temperatures between TPR and in-situ XRD is then probably caused by a higher flowrate during the latter measurements.

### 3.5 TGA/DTA/MS

TGA/DTA profiles of a 20% Co catalyst was compared with a catalyst loaded with 20% Co, 5% Ni. The TGA/DTA profiles of the 20% Co, 5% Ni catalyst can be seen together with their derivatives in figure 3.11. The derivative of the measured mass shows four negative peaks at approx. 75 °C, 180 °C, 255 °C and a wide peak in the region 300-600 °C. These peaks represents mass loss and corresponds with: Evaporation of moisture in the pores, decomposition of residual nitrates in the pores, the first reduction step of cobalt oxide reduction and the second reduction step towards metallic cobalt. Mass spectra of the exhaust was investigated and compared with mass spectra of the support, a

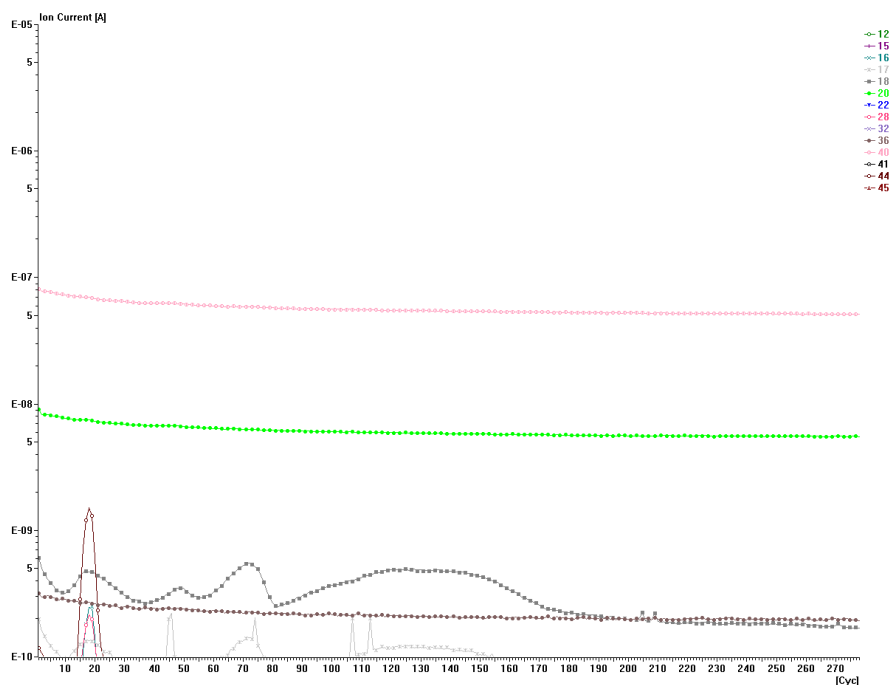


Figure 3.12: *Mass spectroscopy of a 20% Co, 5% Ni catalyst during reduction. Time and temperature increases along the x-axis.*

uncalcinated catalyst and the catalyst under nonreducing conditions. Peaks in water content could be seen clearly for all four reactions. Nitrous gases was detected at 170 °C when heating the uncalcinated catalyst, while ammonia was detected at broader range of temperatures in the other catalysts, indicating conversion of nitrates upon reactions with hydrogen. Figure 3.12 shows the development of MS peaks over time for the 20% Co, 5% Ni catalyst.  $\frac{m}{z}$ -values of 40 and 20 identifies the Ar carrier gas, 18 identifies water, while 17 identifies ammonia. Notice how water content is peaking during the reactions identified from the TGA-curve. When comparing with the 20% Co catalyst, the minima near 255 °C representing the first reduction step was moved to 270 °C, while the other peaks did not show any clear changes. This indicates that nickel promotion decreases the reduction temperature of the first reduction step, but does not affect the second reduction step.

Table 3.3: Measured dispersion and estimated particle size by chemisorption.

Metal loading	Dispersion	Estimated particle size [nm]
20% Co	6.9%	14.4
20% Co, 1% Ni	7.8%	12.8
20% Co, 5% Ni	8.3%	12.0
20% Co, 10% Ni	8.5%	11.8
6.3% Ni	28.1%	3.6
10% Ni	22.9%	4.4

### 3.6 Chemisorption

Dispersion of the catalysts was measured by chemisorption, and particle sizes was estimated assuming spherical particles with a conversion factor of 96. The measured dispersion and estimated particle sizes are shown in table 3.3. The nickel is here shown to be highly dispersed during the first impregnation and calcination. The metal dispersion on the promoted catalysts are also shown to increase with higher nickel content. Much of the increased dispersion seems to be obtainable with low nickel loadings (1%). It should be noted that the measured dispersion does not distinguish between cobalt and nickel, the estimated cobalt particle size could be underestimated depending on the available nickel surface for chemisorption when using this method.

### 3.7 Effect of preparation method

While this thesis focuses on catalysts where nickel was added in the first calcination step, a few catalysts was made with other methods for comparison. Two catalysts loaded with 20% Co and 10% Ni was made by coimpregnation and in two steps with cobalt added first. These catalysts was characterized with chemisorption and TPR. Table 3.4 shows the measured dispersions. The two catalysts that was made in two steps shows small differences in dispersion, while the coimpregnated catalyst had a dispersion equal to an unpromoted 20% cobalt catalyst. Result from the TPR analysis are shown in figure 3.13. Both the coimpregnated catalyst and the catalyst impregnated with nickel in the

Table 3.4: Measured dispersion and estimated particle size by chemisorption for different 20% Co, 10% Ni catalysts.

Impregnation	Dispersion	Estimated particle size [nm]
Ni first	8.5%	11.8
Coimpregnated	6.8%	14.8
Co first	8.7%	11.5

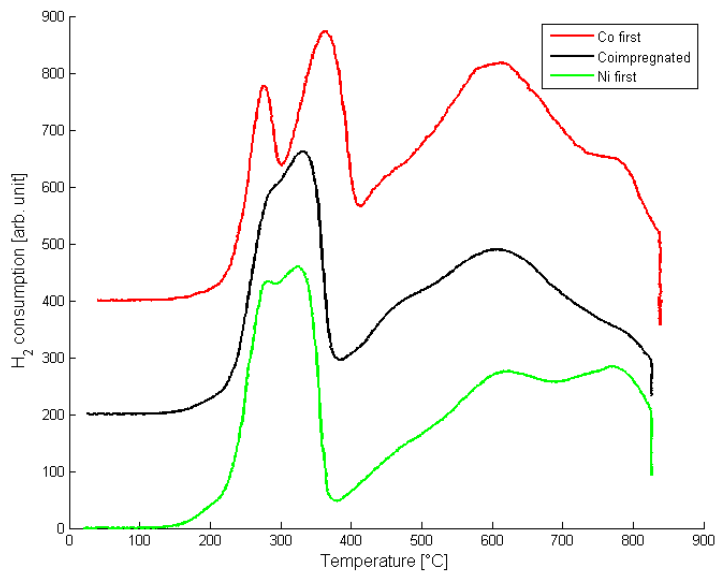


Figure 3.13: Comparison of reduction temperatures for different 20% Co, 10% Ni catalysts.

first have their first reduction peak around 330 °C. The catalyst with cobalt added first had a corresponding reduction peak around 360 °C which equals an unpromoted cobalt catalyst. The reduction temperature of the second reduction step remained equal for all catalysts.

The catalysts dried under vacuum was measured with chemisorption. Compared with catalysts of the same loading made with the incipient wetness method. The coimpregnated catalyst was measured with a higher dispersion (8.6%) than the traditional catalyst (6.2%). On the other hand, no difference in dispersion was observed for the cobalt catalyst (6.7% vs. 6.9%). It is not possible to conclude whether drying under vacuum will increase catalyst dispersion with these results. Because of its status as a new method, the laboratory work had elements of trial and error that may explain the observed differences between the samples. Based on the experiences when making these two catalysts, I will recommend the following changes to the experimental set-up for further development of this method:

- The magnetic stirrer did often get stuck in the wet support. A mechanical stirrer or a rotary evaporator should be used instead.
- A cold trap should be mounted between the round-bottom flask and the vacuum pump to remove moisture.

### 3.8 Effect on reducibility

The effect of promotion with nickel on reducibility is most clearly seen in the results from the TPR. A decrease in the reduction temperature of 40 °C was observed for the first reduction step (reaction 1.9) between a 20% Co catalyst and catalyst with a nickel loading of 5-10%. The observed change in reduction temperature is significant within  $2\sigma$ . The measurements done with TPR does however not show any change in reduction temperature for catalysts with 1% nickel loading, and does not show any variation between catalysts with 5% and 10% nickel loading. This indicates that a minimum loading of nickel somewhere between 1% and 5% is necessary in order to act as a reduction promoter. The possibility of that experimental errors or that the error margins of the used equipment exceeded the possible effect of the 1% nickel catalyst

should however not be disregarded. Nickel promotion was not seen to influence the reduction temperature of the second reduction step (reaction 1.10) in contradiction to claims by Rytter et al. [3]. Reduced reduction temperatures for the first reduction step were also observed by in-situ XRD and TGA/DTA measurements. These observations supports the effect of nickel promotion observed by the TPR measurements. A measurement of a coimpregnated catalyst did also show reduced reduction temperature.

### 3.9 Effect on dispersion

Dispersion and particle size of cobalt are not as easily observed as the reducibility since these properties have been measured and estimated more indirectly (as a ratio between available surface area and loading by chemisorption and the broadening of diffraction peaks by XRD). Since these measurements targets different physical properties, they should not be expected to yield equal values. Clear trends in particle sizes and dispersion should however be measurable by both methods. Chemisorption shows a increase in dispersion for the nickel containing catalysts that corresponds to a decrease of 10% in particle size between 0% and 1% nickel and 20% between 0% and 10% nickel. This indicates that most of the effect of nickel promotion on dispersion is found at loadings below 5%. In-situ XRD shows a decrease of 25% in cobalt particle size between the cobalt catalyst and the catalyst promoted with 10% nickel. The in-situ XRD does also show that nickel promotion decreases cobalt particle sizes by inhibiting sintering during the second reduction step. Even though XRD of the unreduced catalysts indicates that nickel promotion decreases particle sizes for cobalt oxide, these variations should not be used to estimate metal particle sizes in promoted catalysts since effects during reduction seems to be the most influential factor to decrease particle sizes.



# Chapter 4

## Conclusion

In the previous chapters, the effect of nickel promotion of cobalt Fischer-Tropsch catalysts towards reducibility and dispersion were studied and discussed. This study has focused upon catalysts made with a two step method: First impregnation and calcination with nickel, then with cobalt. Catalysts with 20% cobalt and 0-10% nickel loading at a  $\gamma$ -alumina support was made and used during the work. The catalysts were characterized with chemisorption, temperature programmed reduction (TPR) and in- and ex-situ x-ray diffraction (XRD).

The following conclusions are made and supported with the results from the experimental work:

- Promotion with nickel decreases the reduction temperature of the first reduction step of cobalt oxide  $Co_3O_4 \rightarrow CoO$ . No influence was observed towards the second reduction step.
- Promotion with nickel increases dispersion by inhibiting sintering during the second reduction step  $CoO \rightarrow Co$ . Reduced sintering at elevated temperatures was also observed for nickel promoted catalysts.

For further work in this field, I would recommend:

- Investigation of the catalysts with electron microscopy in order to find out how cobalt and nickel particles interacts at the surface of the support.

- Further and more detailed investigation of the catalyst reduction using in-situ XRD with a non-luminescent x-ray source and fast-scanning detector.
- Further investigation of different catalysts with nickel loadings of 1-5% in order to find the most efficient loadings.
- Studies of the catalysts at reaction conditions in order to investigate the effect of nickel promotion on activity and product selectivity.

# Nomenclature

## Latin characters

$a$	Cross-sectional area
$a$	Lattice parameter
$A_S$	Surface area
$B$	Line broadening
$B_{inst}$	Instrument line broadening
$B_{obs}$	Observed line broadening
$C$	BET constant
$D$	Dispersion
$d$	Diameter
$d_{hkl}$	Interplanar spacing
$h$	Miller index
$K$	Scherrer constant
$k$	Miller index
$k_p$	Rate constant of chain propagation
$k_t$	Rate constant of chain termination
$\langle L \rangle$	Mean crystallite thickness

$l$	Miller index
$m$	Mass
$M_n$	Molar mass
$n$	Chain length as number of monomers
$n$	Order of diffraction
$N_A$	Avogadro constant
$p$	Pressure
$p_0$	Probability of initiation of chain growth
$p_0$	Saturation pressure
$p_n$	Probability to make a chain of length $n$
$S_n$	Carbon selectivity
$T$	Temperature
$V_{ads}$	Adsorbed gas volume
$V_m$	Molar volume
$V_{ML}$	Monolayer volume
$w_m$	Weight fraction of metal
$z$	Charge

**Greek characters**

$\alpha$	Probability of chain growth
$\theta$	Bragg angle
$\lambda$	Wave length
$\nu$	Stoichiometric coefficient
$\sigma$	Standard error

**Abbreviations**

Arb. unit	Arbitrary unit
BET	Brunauer-Emmett-Teller
CtL	Coal to liquids
DTA	Differential thermal analysis
GtL	Gas to liquids
HTFT	High temperature Fischer-Tropsch
LTFT	Low temperature Fischer-Tropsch
MS	Mass spectrometry
NTNU	The Norwegian University of Science and Technology
SASOL	Suid Afrikaanse Steenkool en Olie
TGA	Thermal gravimetric analysis
TOF	Turn over frequency
TPR	Temperature programmed reduction
WGS	Water-gas shift
XRD	X-ray diffraction



# Bibliography

- [1] Borg Ø. Role of Alumina Support in Cobalt Fischer-Tropsch Synthesis. Norwegian University of Science and Technology. Trondheim; 2007.
- [2] Diehl F, Khodakov AY. Promotion of Cobalt Fischer-Tropsch Catalysts with Noble Metals: a Review. *Oil & Gas Science and Technology - Rev IFP*. 2009;64:11–24.
- [3] Rytter E, Skagseth TH, Eri S, Sjøstad AO. Cobalt Fischer-Tropsch Catalysts Using Nickel Promoter as a Rhenium Substitute to Suppress Deactivation. *Ind Eng Chem Res*. 2010;49:4140–4148.
- [4] Stranges AN. A history of the Fischer-Tropsch Synthesis in Germany 1926-45. In: Davis BH, Ocelli ML, editors. *Fischer-Tropsch synthesis, catalysts and catalysis*. vol. 163 of *Studies in Surface Science and Catalysis*. Amsterdam: Elsevier; 2007. .
- [5] Dancuart LP, Steynberg AP. Fischer-Tropsch based GTL Technology: a New Process? In: Davis BH, Ocelli ML, editors. *Fischer-Tropsch synthesis, catalysts and catalysis*. vol. 163 of *Studies in Surface Science and Catalysis*. Amsterdam: Elsevier; 2007. .
- [6] Moulijn JA, Makkee M, van Diepen A. *Chemical Process Technology*. Chichester: John Wiley & Sons; 2001.
- [7] Sie ST, Senden MMG, van Wechem HMH. Conversion of natural gas to transportation fuels via the Shell middle distillate synthesis process (SMDS). *Catalysis Today*. 1991;8:371–394.
- [8] Holmen A. *Heterogen katalyse*. Trondheim: Department of Chemical Engineering, NTNU;. *Compendium*.

- [9] Khodakov AY, Chu W, Fongarland P. Advances in the Development of Novel Cobalt Fischer-Tropsch Catalysts for Synthesis of Long-Chain Hydrocarbons and Clean Fuels. *Chem Rev.* 2007;107:1692–1744.
- [10] Dry ME. High quality diesel via the Fischer-Tropsch process - a review. *J Chem Technol Biotechnol.* 2001;77:43–50.
- [11] Bao B, El-Halwagi MM, Elbashir NO. Simulation, integration, and economic analysis of gas-to-liquid processes. *Fuel Processing Technology.* 2010;91:703–713.
- [12] Vannice MA. The Catalytic Synthesis of Hydrocarbons from H<sub>2</sub>/CO Mixtures over the Group VIII Metals - I. The Specific Activities and Product Distributions of Supported Metals. *J Catal.* 1975;37:449–461.
- [13] Jacobs G, Das TK, Zhang Y, Li J, Racoillet G, Davis BH. Fischer-Tropsch synthesis: support, loading, and promoter effects on the reducibility of cobalt catalysts. *Applied Catalysis A: General.* 2002;233:263–281.
- [14] Ishihara T, Eguchi K, Arai H. Hydrogenation of carbon monoxide over SiO<sub>2</sub>-supported Fe-Co, Co-Ni and Ni-Fe bimetallic catalysts. *Applied Catalysis.* 1987;30:225–238.
- [15] Ishihara T, Eguchi K, Arai H. Supported Iron-Cobalt-Nickel Ternary Alloy Catalysts for the Hydrogenation of Carbon Monoxide. *Applied Catalysis.* 1988;40:87–100.
- [16] Ishihara T, Horiuchi N, Inoue T, Eguchi K, Takita Y, Arai H. Effect of Alloying on CO Hydrogenation activity over SiO<sub>2</sub>-Supported Co-Ni Alloy Catalysts. *J Catal.* 1992;136:232–241.
- [17] Horiuchi N, Ishihara T, Eguchi K, Arai H. Hydrogenation of Carbon Monoxide over Mixed Oxide Supported 50Co50Ni Alloy Catalysts. *Chemistry Letters.* 1988;p. 499–502.
- [18] Fan L, Yoshii K, Yan S, Zhou J, Fujimoto K. Supercritical-phase process for selective synthesis of wax from syngas: Catalyst and process development. *Catalysis Today.* 1997;36:295–304.
- [19] Rytter E, Eri S, Schanke D, Wigum H, Hulsund T, Borg Ø, et al. Development of an Attrition Resistant Fischer-Tropsch Catalyst for Slurry Operation. *Top Catal.* 2011;54:801–810.

- [20] Enger BC, Fossan ÅL, Borg Ø, Rytter E, Holmen A. Modified alumina as catalyst support for cobalt in the Fischer-Tropsch synthesis. *J Catal.* 2011;284:9–22.
- [21] Richardson JT. *Principles of Catalyst Development. Fundamental and Applied Catalysis.* New York: Plenum Press; 1989.
- [22] Fafet A. In: Lynch J, editor. *Thermal Analysis Methods.* Paris: Editions Technip; 2003. .
- [23] Anderson JR, Pratt KC. *Introduction to characterization and testing of catalysts.* Academic press; 1985.
- [24] Smith RM. *Understanding Mass Spectra: A Basic Approach.* 2nd ed. Hoboken: John Wiley & Sons; 2004.
- [25] Constantin E, Schnell A. *Mass spectrometry.* Chichester: Ellis Horwood; 1990.
- [26] Callister jr WD. *Materials Science and Engineering - An Introduction.* 7th ed. New York: John Wiley & Sons; 2007.
- [27] Borg Ø, Eri S, Rytter E, Holmen A. Fischer-Tropsch synthesis over different alumina supported cobalt catalysts. *Prepr Pap - Am Chem Soc, Div Fuel Chem.* 2006;51:699–701.
- [28] Paulus EF, Gieren A. *Structure Analysis by Diffraction.* In: *Ullmann's Encyclopedia of Industrial Chemistry.* Weinheim: John Wiley & Sons; 2005. .
- [29] Mørk PC. *Overflate og koloidkjemi - Grunnleggende prinsipper og teorier.* 8th ed. Trondheim: Department of Chemical Engineering, NTNU; 2004.
- [30] Vannice MA. *Kinetics of Catalytic Reactions.* New York: Springer; 2005.
- [31] Anderson JA, Fernandez-Garcia M, Martínez-Arias A. Determination of Dispersion and Supported Metal Crystallite Size. In: Anderson JA, García MF, editors. *Supported Metals in Catalysis.* vol. 5 of *Catalytic Science Series.* London: Imperial College Press; 2005. .
- [32] Rane SP. *Relation Between Catalyst Properties and Selectivity in Fischer-Tropsch Synthesis.* Norwegian University of Science and Technology. Trondheim; 2011.

- [33] Borg Ø, Eri S, Blekkan EA, Storsæter S, Wigum H, Rytter E, et al. Fischer-Tropsch synthesis over  $\gamma$ -alumina-supported cobalt catalysts: Effect of support variables. *J Catal.* 2007;248:89–100.
- [34] Aylward G, Findlay T. *SI Chemical Data*. 5th ed. Milton: John Wiley & Sons; 2002.

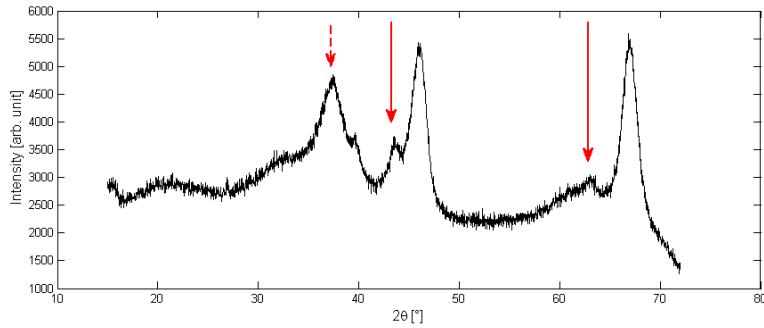
# Appendix A

## Peak fitting of $\gamma$ -Al<sub>2</sub>O<sub>3</sub> supports in TOPAS

This appendix describes the method used for peak fitting of catalysts with  $\gamma$ -alumina support during the data analysis work done for this thesis. As this method is (to my knowledge) not published or documented anywhere else, I have decided to give a brief step-by-step description on how to use this method in the Bruker Topas 4.2 software. I want to thank dr. Julian Tolchard at the Department of Material Science and Engineering, NTNU for coming up with, and learning me, this method.

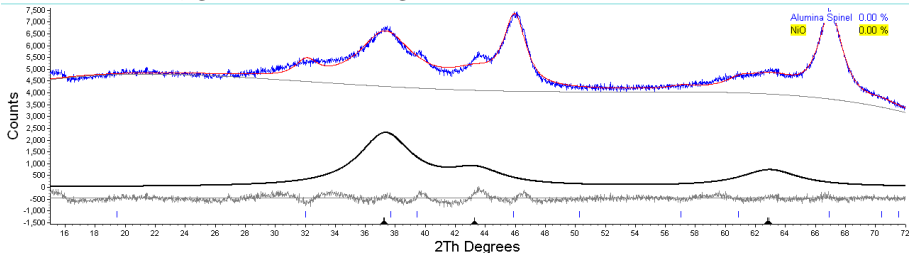
### Problem description

A 10% Ni catalyst with a  $\gamma$ -alumina support was investigated in a Bruker D8 advance diffractometer and scanned with  $2\theta$  in the range of 15°-72°, a step size of 0.0245° and a measurement time of 1.2 s/step. A diffractogram of the unreduced catalyst is shown below:

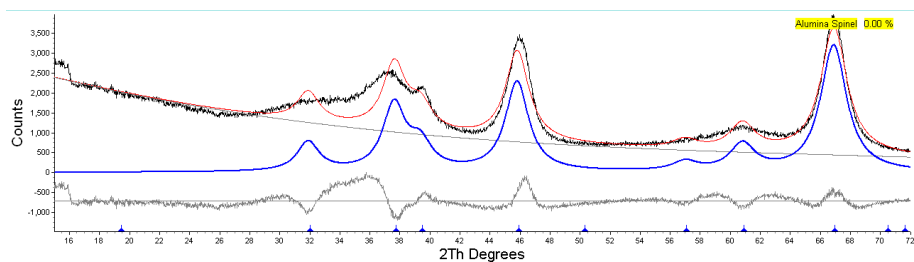


The red arrows marks the visible NiO peaks (at  $43.3^\circ$  and  $62.9^\circ$ ), while the dotted arrow marks an additional peak which are overlapping with a  $\gamma$ - $Al_2O_3$  peak at  $37.3^\circ$ .

When analysed in TOPAS, peak positions are calculated theroretically and the different phases are found by fitting the diffractogram to the calculated peaks numerically. Fitting the diffractogram shown above to a model of  $\gamma$ - $Al_2O_3$  and NiO in TOPAS, gives the following result:



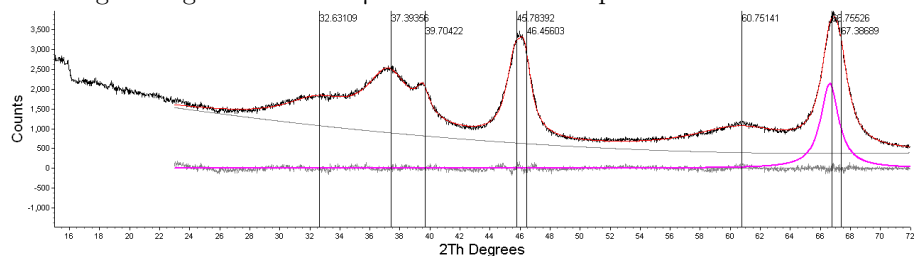
The red curve show the how the software fits the diffractogram (in blue). While the black line beneath represents where TOPAS did calculate the NiO peaks. The grey line at bottom shows the differece between the fitted values calculated by TOPAS and the diffractogram which gives an easy to understand hint about the quality of the fit. The fitted values of the NiO phase shows that TOPAS fails to fit the most distinctive NiO peak at  $43.3^\circ$ , while treating the peak at  $37.3^\circ$  (which is maily caused by  $\gamma$ - $Al_2O_3$ ) as a NiO peak. While trying to fit a diffractogram of the  $\gamma$ - $Al_2O_3$  to its theoretical values, the following fit is achieved:



Which is even worse than the one with NiO. It should be obvious that the normal approach is not suited for this support.

## How to fit

In order to get a good fit of the  $\gamma$ -alumina, it could be modelled as a peak phase. This is done by importing a diffractogram with the support only in a new TOPAS project. Add a peak phase to the diffractogram by right clicking and choose “Add peak phase”. Peaks should then be placed at suitable positions until it gives a good fit of the  $\gamma$ -alumina. An example is shown below:



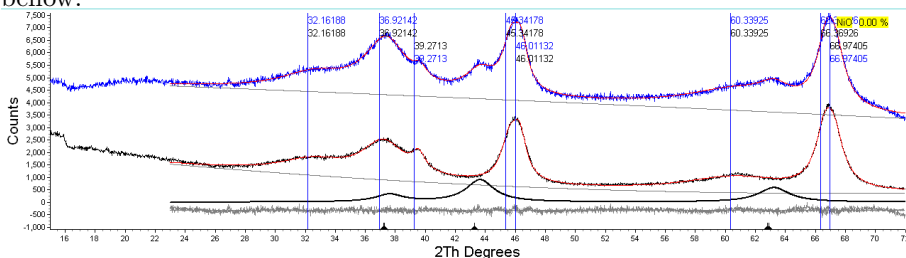
These eight peaks are shown to give a good fit of the support. The peak in pink shows the contribution of the  $66.8^\circ$  peak (the whole peak is modelled as a superposition of two peaks). It is important to make sure that every peak in the peak phase matches a peak in the diffractogram in some way. If not, these peaks could fit the background radiation and become an error source.

In order to use this fit in another diffractogram, one marks the peak phase and chooses “Codes” and assigns unique variable names for the position and crystallite size of each peak:

Values	Codes	Errors	Min	Max	LVolHB (nm)	LVolFWHM (nm)	e0	Additional Convolutions	Rpt/Text		
Type	Use	Position	Position	Area	Use	Cry size L (nm)	Use	Cry size G	Use	Strai	
1	FP	<input checked="" type="checkbox"/>	32.63109	Al_30_Pos_1	Refine	<input checked="" type="checkbox"/>	Al_30_Cry_1	<input type="checkbox"/>	Refine	<input type="checkbox"/>	Refir
2	FP	<input checked="" type="checkbox"/>	37.39356	Al_30_Pos_2	Refine	<input checked="" type="checkbox"/>	Al_30_Cry_2	<input type="checkbox"/>	Refine	<input type="checkbox"/>	Refir
3	FP	<input checked="" type="checkbox"/>	39.70422	Al_30_Pos_3	Refine	<input checked="" type="checkbox"/>	Al_30_Cry_3	<input type="checkbox"/>	Refine	<input type="checkbox"/>	Refir
4	FP	<input checked="" type="checkbox"/>	45.78392	Al_30_Pos_4	Refine	<input checked="" type="checkbox"/>	Al_30_Cry_4	<input type="checkbox"/>	Refine	<input type="checkbox"/>	Refir
5	FP	<input checked="" type="checkbox"/>	46.45603	Al_30_Pos_5	Refine	<input checked="" type="checkbox"/>	Al_30_Cry_5	<input type="checkbox"/>	Refine	<input type="checkbox"/>	Refir
6	FP	<input checked="" type="checkbox"/>	60.75141	Al_30_Pos_6	Refine	<input checked="" type="checkbox"/>	Al_30_Cry_6	<input type="checkbox"/>	Refine	<input type="checkbox"/>	Refir
7	FP	<input checked="" type="checkbox"/>	66.75526	Al_30_Pos_7	Refine	<input checked="" type="checkbox"/>	Al_30_Cry_7	<input type="checkbox"/>	Refine	<input type="checkbox"/>	Refir
8	FP	<input checked="" type="checkbox"/>	67.38689	Al_30_Pos_8	Refine	<input checked="" type="checkbox"/>	Al_30_Cry_8	<input type="checkbox"/>	Refine	<input type="checkbox"/>	Refir

In this example, the variable names starts with “Al\_30\_Pos\_” and “Al\_30\_Cry\_”. The peak phase is then saved (with the variable names) by right clicking the phase and choose “Save phase”. The diffractogram with NiO is then imported to the TOPAS project. Import the saved phase into this diffractogram and make or import a structure with NiO. Open the peak phase and put a “=”-sign in front of each variable name<sup>1</sup>. The peak phases representing  $\gamma$ - $Al_2O_3$  in both diffractograms are now linked together in such a way that the fit calculated for the diffractogram of the support will be used to distinguish between the support and NiO in the other diffractogram.

Before one starts de calculations, it is recommended to lock the values of the variables linking the diffractograms. This is done by opening the peak phase in the support diffractogram and double click at the variable names before fitting both diffractograms. Then unlock the variables and fit the second time when the peaks are allowed to change in order to give a better fit. The result is shown bellow:



This is a lot better than the first attempt. Diffractogram of the support is shown in black, while the one with NiO is shown in blue above.

<sup>1</sup>Not strictly necessary, but could prevent a lot of errors.

# Appendix B

## Examples of calculations

### Catalyst preparation

A 20% Co, 5% Ni catalyst is used as an example. First, the metal content of the precursor salts was calculated. The values used were found in *SI Chemical Data* [34]:

$$\frac{m_{Co}}{m_{salt}} = \frac{M_{n,Co}}{M_{n,salt}} = \frac{58.93}{58.93 + 2(14.01 + 3 \cdot 16.00) + 6 \cdot 18.01} = 0.203$$

$$\frac{m_{Ni}}{m_{salt}} = \frac{M_{n,Ni}}{M_{n,salt}} = \frac{58.69}{58.69 + 2(14.01 + 3 \cdot 16.00) + 6 \cdot 18.01} = 0.202$$

In order to make 10 g of catalyst, the amount of support needed is:

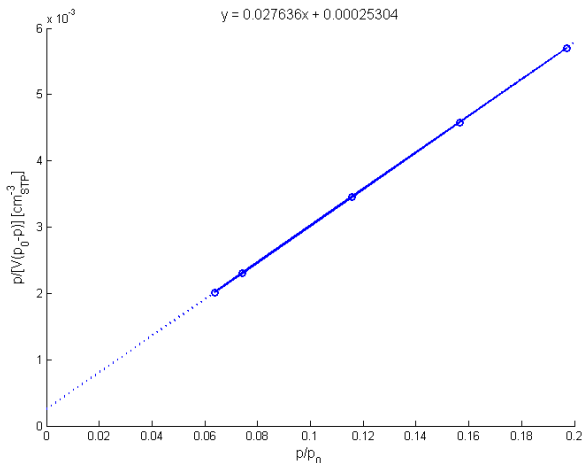
$$m_{support} = 10(1 - 0.20 - 0.05) = 7.50g$$

The amount of salt needed is then:

$$m_{salt,Co} = \frac{10 \cdot 0.20}{0.203} = 9.85g$$

$$m_{salt,Ni} = \frac{10 \cdot 0.05}{0.202} = 2.48g$$

Assuming a wetness point of 1.3273 for the fresh support, the needed amount of water is then (only calculated for Ni since the exact wetness point for Ni

Figure B.1: *Example of BET isotherm.*

catalysts are unknown, see section 2.1):

$$m_{H_2O} = 7.50 \cdot 1.3273 = 9.95g$$

The amount of crystal water in the salts must however be calculated and subtracted from this number:

$$\frac{m_{H_2O, salt}}{m_{salt}} = \frac{6 \cdot 18.01}{58.69 + 2(14.01 + 3 \cdot 16.00) + 6 \cdot 18.01} = 0.372$$

$$m_{H_2O} = 9.95 - 2.48 \cdot 0.372 = 9.03g$$

Then: 2.48 g of  $Ni(NO_3)_2 \cdot 6H_2O$  must be soluted in 9.03 g of water in the first impregnation step, while 9.85 g of  $Co(NO_3)_2 \cdot 6H_2O$  is used in the second impregnation.

## Physisorption

A measurement of sample 17A (the support) is used to calculate the surface area with the BET method. Values for pressure, saturation pressure and adsorbed gas volume are plotted together in a linear plot in figure B.1. A linear curve

fit to equation 1.16 gives:

$$\frac{C-1}{V_{ML}C} = 0.02764 \frac{g}{cm^3_{STP}}$$

$$\frac{1}{V_{ML}C} = 0.00025 \frac{g}{cm^3_{STP}}$$

The monolayer coverage is found by:

$$\frac{C-1}{V_{ML}C} + \frac{1}{V_{ML}C} = \frac{C-1+1}{V_{ML}C} = \frac{1}{V_{ML}}$$

$$\implies V_{ML} = \frac{1}{0.02764 + 0.00025} = 35.855 \frac{cm^3_{STP}}{g}$$

Assuming a cross sectional area of  $0.1620 \text{ nm}^2$  per molecule, the surface area is calculated with equation 1.17:

$$A = \frac{V_{ML}aN_A}{V_m} = \frac{35.855 \cdot 1.62 \cdot 10^{-19} \cdot 6.022 \cdot 10^{23}}{22400} = 156 \frac{m^2}{g}$$

## Chemisorption

A measurement of sample 19D (20% Co, 5% Ni) is used to calculate the dispersion. The adsorbed gas volume is found to be  $4.0245 \text{ cm}^3_{STP}/g$  by linear interpolation of the first adsorption isotherm toward zero pressure (the curve fitting tool in MATLAB was used in this case) as shown in figure B.2. Assuming that  $H_2$  adsorption has a stoichiometric factor of 2 on both metals, equation 1.18 takes the form:

$$D = \frac{V_{ads}\nu}{\frac{w_{Co}}{M_{n,Co}} + \frac{w_{Ni}}{M_{n,Ni}}} = \frac{1}{22414} \cdot \frac{4.0245}{\frac{0.20}{58.93} + \frac{0.05}{58.69}} = 0.0846 \approx 8\%$$

Where  $1/22414$  is a conversion factor from  $cm^3_{STP}$  to mol. Using a shape factor of 96, the particle size is estimated:

$$d = \frac{96}{8} = 12 \text{ nm}$$

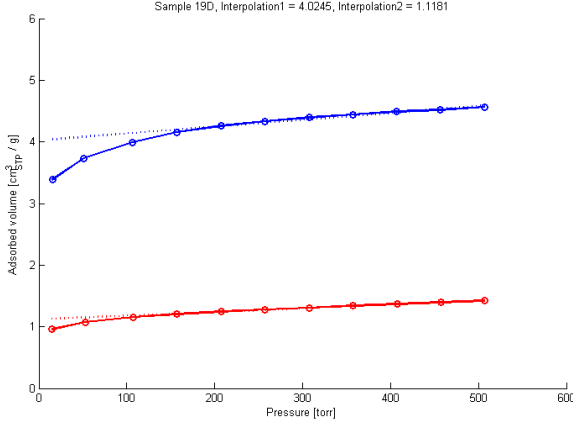


Figure B.2: *Adsorption isotherms and interpolation of sample 19D.*

## XRD

The particle size of cobalt oxide ( $\text{Co}_3\text{O}_4$ ) in sample 19D is calculated with the Scherrer equation. The peak near  $2\theta = 59^\circ$  is chosen for this example since its overlap with the support seems to be insignificant. The baseline is assumed to be at an intensity of 30, while the peak height was found to be 156.9. This gives a half height of 78.5 with a corresponding width of 0.0135 rad. These values are shown in figure B.3. The instrument line broadening is assumed to be 0.0013 rad at this point. The correct peak width is calculated according to equation 1.15:

$$B = \sqrt{B_{obs}^2 - B_{inst}^2} = \sqrt{0.0135^2 - 0.0013^2} = 0.0134 \text{ rad}$$

The instrument line broadening seems to be neglectable in this case. The mean crystallite thickness is then calculated from equation 1.14 using a Scherrer constant of 0.89, a x-ray wavelength of 0.154 nm and a bragg angle of  $\frac{59.2}{2} = 29.6^\circ = 0.5166 \text{ rad}$ :

$$\langle L \rangle = \langle L \rangle = \frac{K\lambda}{B \cos \theta} = \frac{0.89 \cdot 0.154}{0.0134 \cos 0.5166} = 11.76 \text{ nm}$$

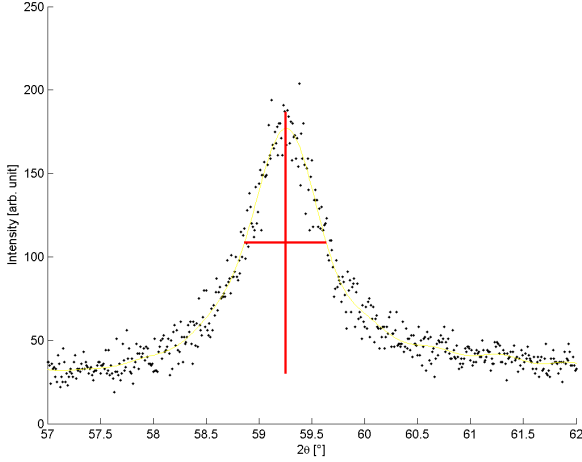


Figure B.3: *Example of peak. The peak height and half height width used in the calculations shown as red lines.*

## Calculation of lattice parameters

Lattice parameters of a crystalline solid can be calculated from the peak positions in a x-ray diffractogram. As lattice parameters change during heating due to thermal expansion, such calculations may be necessary when investigating diffractograms from in-situ studies at elevated temperatures. In this example, the  $[1,1,1]$  peak of fcc-Co is investigated in diffractograms taken at 500 °C and 850 °C. At 500 °C, the peak is located at  $2\theta = 44.0^\circ$ . At 850 °C, the peak position has moved to  $2\theta = 43.6^\circ$ . The interplanar spacing is then calculated assuming the peak to be of the first order of diffraction and a wavelength of 0.154 nm:

$$d_{hkl,500^\circ C} = \frac{n\lambda}{2 \sin \theta} = \frac{1 \cdot 0.154}{2 \sin(\frac{44.0}{2})} = 0.2055 \text{ nm}$$

$$d_{hkl,850^\circ C} = \frac{n\lambda}{2 \sin \theta} = \frac{1 \cdot 0.154}{2 \sin(\frac{43.6}{2})} = 0.2073 \text{ nm}$$

With  $h = k = l = 1$ , the lattice parameters can be calculated with equation 1.13:

$$a_{500^\circ C} = d_{hkl,500^\circ C} \sqrt{h^2 + k^2 + l^2} = 0.2055 \sqrt{3} = 0.3559 \text{ nm}$$

$$a_{850^\circ C} = d_{hkl,850^\circ C} \sqrt{h^2 + k^2 + l^2} = 0.2073 \sqrt{3} = 0.3591 \text{ nm}$$



# Appendix C

## Additional data and results

Table C.1: List of samples made during the thesis work. The samples are named by a conversion where they are given a number and a single letter suffix that increases each time the catalyst has been changed anyway i.e. A after the first impregnation, B after the first calcination, C after the second impregnation and so on.

Sample	Metal loading	Support	Impregnation	Comments
16D	20% Co, 5% Ni	$\gamma$ -Al <sub>2</sub> O <sub>3</sub>	Ni first	Test catalyst. Produced with low purity salts. Not used.
17A	-	$\gamma$ -Al <sub>2</sub> O <sub>3</sub>	-	Sample of support only.
17B	-	$\gamma$ -Al <sub>2</sub> O <sub>3</sub>	-	Support heated to 900 °C
18D	20% Co, 1% Ni	$\gamma$ -Al <sub>2</sub> O <sub>3</sub>	Ni first	Lost air stream during calcination. Assumed to be spoiled. Not used.
19B	6.3% Ni	$\gamma$ -Al <sub>2</sub> O <sub>3</sub>	Ni	Precursor of sample 19D. Taken aside after 1st calcination.
19D	20% Co, 5% Ni	$\gamma$ -Al <sub>2</sub> O <sub>3</sub>	Ni first	
20D	20% Co, 1% Ni	$\gamma$ -Al <sub>2</sub> O <sub>3</sub>	Ni first	
21D	20% Co, 10% Ni	$\gamma$ -Al <sub>2</sub> O <sub>3</sub>	Ni first	
21E	20% Co, 10% Ni	$\gamma$ -Al <sub>2</sub> O <sub>3</sub>	Ni first	Heated to 900 °C during in-situ XRD study.
22B	20% Co	$\gamma$ -Al <sub>2</sub> O <sub>3</sub>	Co	
22C	20% Co	$\gamma$ -Al <sub>2</sub> O <sub>3</sub>	Co	Heated to 900 °C during in-situ XRD study.
23D	20% Co, 5% Ni	$\gamma$ -Al <sub>2</sub> O <sub>3</sub>	Ni first	
25B	20% Co, 10% Ni	$\gamma$ -Al <sub>2</sub> O <sub>3</sub>	Coimpregnated	
26B	20% Co	$\gamma$ -Al <sub>2</sub> O <sub>3</sub>	Co	
27B	10% Ni	$\gamma$ -Al <sub>2</sub> O <sub>3</sub>	Ni	
28C	10% Co, 1% Ni	$\gamma$ -Al <sub>2</sub> O <sub>3</sub>	Ni first	Not calcined after impregnation with Co.
28D	10% Co, 1% Ni	$\gamma$ -Al <sub>2</sub> O <sub>3</sub>	Ni first	28C calcined.
29D	20% Co, 10% Ni	$\gamma$ -Al <sub>2</sub> O <sub>3</sub>	Co first	Too dry after impregnation with Co.
30D	20% Co, 10% Ni	$\gamma$ -Al <sub>2</sub> O <sub>3</sub>	Co first	
31B	11% Co, 5% Ni	$\gamma$ -Al <sub>2</sub> O <sub>3</sub>	Coimpregnated	Dried under vacuum.
32B	20% Co, 5% Ni	$\gamma$ -Al <sub>2</sub> O <sub>3</sub>	Coimpregnated	
33B	20% Co	$\gamma$ -Al <sub>2</sub> O <sub>3</sub>	Co	Dried under vacuum.

Table C.2: Surface areas measured by physisorption.

Sample	Composition	Surface area [ $m^2/g$ ]
17A	Support only	148.49
17A	Support only	156.09
17A	Support only	157.76
17B	Support only	63.04
17B	Support only	65.96
19B	6.3% Ni	135.52
19D	20% Co, 5% Ni	105.52
20D	20% Co, 1% Ni	106.59
21D	20% Co, 10% Ni	104.06
21D	20% Co, 10% Ni	108.13
21E	20% Co, 10% Ni	101.78
22B	20% Co	119.77
22C	20% Co	113.06
23D	20% Co, 5% Ni	112.48
26B	20% Co	119.28

Table C.3: Observed peaks in XRD ( $2\theta$ )

$\gamma$ -Al <sub>2</sub> O <sub>3</sub>	$\delta$ -Al <sub>2</sub> O <sub>3</sub>	Co <sub>3</sub> O <sub>4</sub>	NiO	CoO	fcc-Co	fcc-Ni
19.3°	32.6°	18.9°	43.4°	36.5°	44.4°	44.8°
32.1°		31.2°	63.0°	42.6°	51.6°	52.0°
37.0°		36.8°		61.6°		
39.3°		38.4°				
46.0°		44.7°				
60.8°		55.6°				
66.8°		59.2°				
85.0°		65.2°				
		77.3°				
		82.6°				
		90.8°				
		94.0°				

Table C.4: Particle sizes of metal oxide particles calculated with the Scherrer equation.

Sample	Composition	Crystallite size $\langle L \rangle$ [nm]		Particle size (d) [nm]	
		IB	FWHM	IB	FWHM
16D	20% Co, 5% Ni	8.84	12.36	11.79	16.48
18D	20% Co, 1% Ni	9.73	13.61	12.97	18.15
19B	6.3% Ni	1.50	2.09	2.00	2.79
19D	20% Co, 5% Ni	9.73	13.11	12.97	17.48
20D	20% Co, 1% Ni	10.06	14.07	13.41	18.76
21D	20% Co, 10% Ni	8.91	12.45	11.88	16.60
21D	20% Co, 10% Ni	9.17	12.82	12.22	17.09
22B	20% Co	9.59	13.41	12.79	17.88
22B	20% Co	9.37	13.10	12.49	17.47
25B	20% Co, 10% Ni	9.87	13.80	13.16	18.40
25B	20% Co, 10% Ni	9.97	13.94	13.29	18.59
26B	20% Co	10.35	14.47	13.80	19.29
27B	10% Ni	2.59	3.63	3.46	4.83

Table C.5: Calculated particle sizes, in-situ XRD reduction of sample 22B at 350 °C for 16 h.

Temperature [°C]	Co <sub>3</sub> O <sub>4</sub> <L> [nm]		CoO <L> [nm]		fcc-Co <L> [nm]		Co <sub>3</sub> O <sub>4</sub> (d) [nm]		CoO (d) [nm]		fcc-Co (d) [nm]	
	IB	FWHM	IB	FWHM	IB	FWHM	IB	FWHM	IB	FWHM	IB	FWHM
30	10.05	13.8					13.4	18.4				
350			2.8	3.9	9.7	13.6			3.7	5.2	12.9	18.1
350					7.0	9.7					9.3	12.9
350					7.4	10.3					9.9	12.7
350					7.0	9.77					9.3	13.0
30					7.9	11.0					10.5	14.7

Table C.6: Calculated particle sizes, in-situ XRD reduction of sample 21D at 350 °C for 16 h.

Temperature [°C]	Co <sub>3</sub> O <sub>4</sub> <L> [nm]		CoO <L> [nm]		fcc-Co <L> [nm]		Co <sub>3</sub> O <sub>4</sub> (d) [nm]		CoO (d) [nm]		fcc-Co (d) [nm]	
	IB	FWHM	IB	FWHM	IB	FWHM	IB	FWHM	IB	FWHM	IB	FWHM
30	9.49	13.08					12.65	17.44				
350			3.4	4.8	6.0	8.4			4.5	6.4	8.0	11.2
350					5.39	7.53					7.19	10.04
350					6.02	8.42					8.03	11.23
350					5.70	7.97					7.60	10.63
30					5.96	8.33					7.95	11.11

Table C.7: Calculated particle sizes, in-situ XRD reduction of sample 22B to 900 °C.

Temperature [°C]	Co <sub>3</sub> O <sub>4</sub> <L> [nm]		CoO <L> [nm]		fcc-Co <L> [nm]		Co <sub>3</sub> O <sub>4</sub> (d) [nm]		CoO (d) [nm]		fcc-Co (d) [nm]	
	IB	FWHM	IB	FWHM	IB	FWHM	IB	FWHM	IB	FWHM	IB	FWHM
30	10.05	13.8					13.40	18.4				
150	10.39	14.52					13.85	19.36				
200			6.53	8.08					8.71	10.78		
250			5.9	8.2	12.0	11.7			7.9	10.9	16.0	15.6
300			5.2	7.3	9.7	13			6.9	9.7	12.9	17.3
350					6.7	9.4					8.9	12.5
400			2.7	2.6	9.5	12.8			3.6	3.4	12.7	17.1
450					8.2	11.5				10.9	15.3	
500					9.2	12.9				12.3	17.2	
550					9.8	13.7				13.1	18.3	
600					11.0	15.4				14.7	20.1	
650					11.6	16.1				15.5	21.5	
700					12.3	17.2				16.4	22.9	
750					13.7	19.1				18.3	25.5	
800					14.49	19.2				19.32	25.6	
850					16.8	23.5				22.4	31.3	
900					18.7	26.2				24.9	34.9	
30					20.0	27.9				26.7	37.2	

Table C.8: Calculated particle sizes, in-situ XRD reduction of sample 21D to 900 °C.

Temperature [°C]	Co <sub>3</sub> O <sub>4</sub> <L> [nm]		CoO <L> [nm]		fcc-Co <L> [nm]		Co <sub>3</sub> O <sub>4</sub> (d) [nm]		CoO (d) [nm]		fcc-Co (d) [nm]	
	IB	FWHM	IB	FWHM	IB	FWHM	IB	FWHM	IB	FWHM	IB	FWHM
30	9.49	13.08					12.65	17.44				
150	8.6	12.0	5.32	7.44			11.47	16.0	7.09	9.92		
200			5.46	7.63	6.0	8.4			7.28	10.17	8.0	11.2
250			4.7	6.6	6.2	8.7			6.3	8.8	8.3	11.6
300			6.1	5.8	5.6	7.9			8.1	7.7	7.5	10.5
350			2.0	2.6	5.5	7.68			2.7	3.5	7.3	10.24
400					5.24	7.33					6.99	9.77
450					5.72	7.99					7.63	10.65
500					5.53	7.74					7.37	10.32
550					6.35	8.88					8.47	11.84
600					6.38	8.91					8.51	11.88
650					6.78	9.48					9.04	12.64
700					6.86	9.59					9.15	12.79
750					7.70	10.76					10.27	14.35
800					7.87	11.01					10.49	14.68
850					8.64	12.07					11.52	16.09
900					10.40	14.46					13.87	19.28
30					11.16	15.59					14.88	20.79

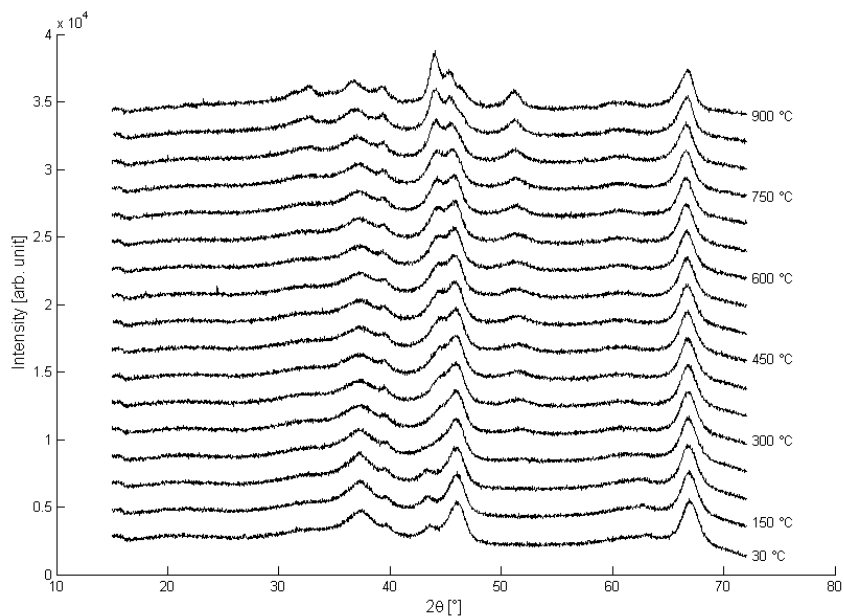


Figure C.1: *In-situ* XRD of sample 27B (10% Ni) while heating to 900 °C under reduction conditions.

Table C.9: Calculated particle sizes, in-situ XRD reduction of sample 27B to 900 °C.

Temperature [°C]	NiO <L> [nm]		fcc-Ni <L> [nm]		NiO (d) [nm]		fcc-Ni (d) [nm]	
	IB	FWHM	IB	FWHM	IB	FWHM	IB	FWHM
30	2.63	3.67			3.51	4.89		
150	2.66	3.58			3.55	4.77		
200	2.45	3.42			3.27	4.56		
250	2.47	2.34	3.60	3.39	3.29	3.12	4.80	4.52
300			3.07	2.91			4.09	3.88
350			1.84	2.34			2.45	3.12
400			2.93	3.56			3.91	4.75
450			3.57	3.39			4.76	4.52
500			3.75	3.57			5.00	4.76
550			3.38	3.61			4.51	4.81
600			3.93	3.92			5.24	5.23
650			3.40	4.55			4.53	6.07
700			4.44	4.21			5.92	5.61
750			4.67	4.42			6.23	5.89
800			5.25	4.98			7.00	6.64
850			4.77	6.65			6.36	8.87
900			7.66	7.26			10.21	9.68
30			7.58	7.19			10.11	9.59

Table C.10: Identified  $\frac{m}{z}$ -values from mass spectra

$\frac{m}{z}$	Substance
2	H <sub>2</sub>
17	NH <sub>3</sub>
18	H <sub>2</sub> O
20	Ar
28	N <sub>2</sub>
30	NO
40	Ar

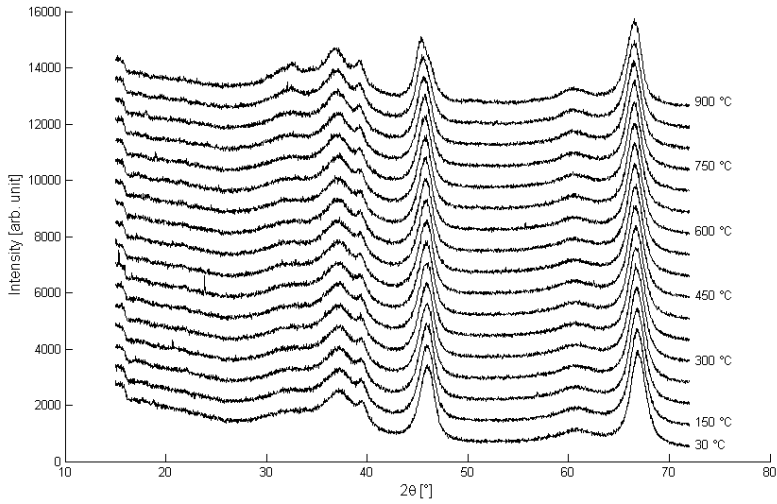


Figure C.2: *In-situ* XRD of sample 17A ( $\gamma\text{-Al}_2\text{O}_3$ ) while heated to 900 °C in a  $\text{H}_2/\text{N}_2$  atmosphere.

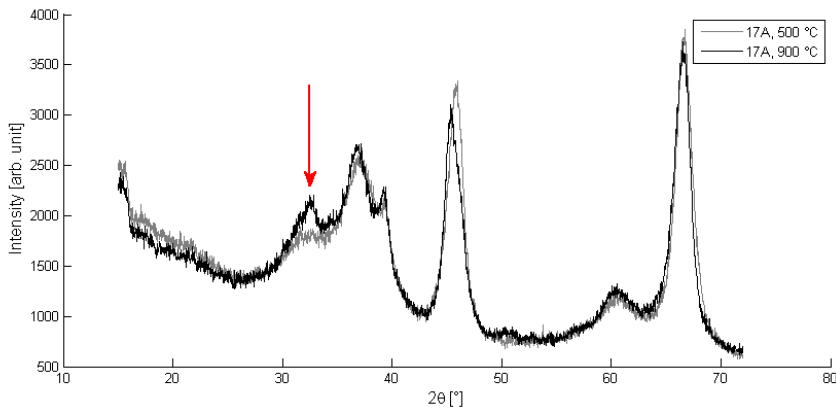


Figure C.3:  $\delta\text{-Al}_2\text{O}_3$  peak shown while comparing diffractograms of sample 17A taken at 500 °C (grey) and 900 °C (black).

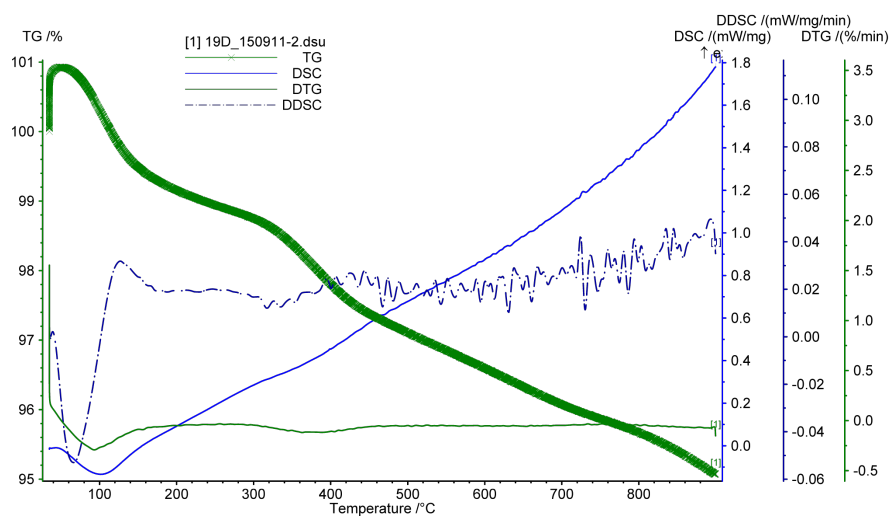


Figure C.4: Sample 19D (20% Co, 5% Ni) heated in an Ar-atmosphere.

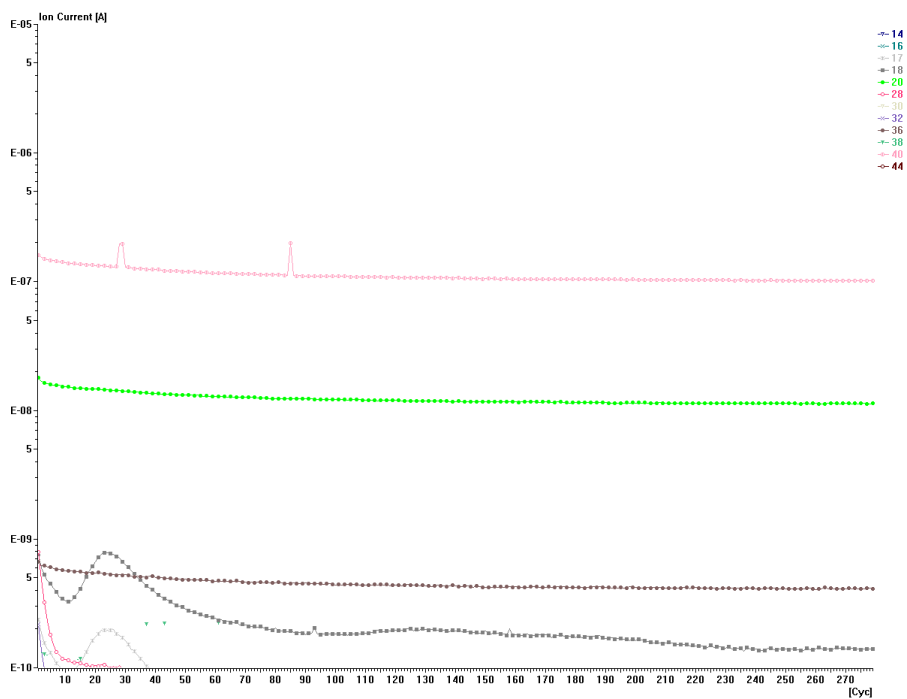


Figure C.5: Sample 19D (20% Co, 5% Ni) heated in an Ar-atmosphere (see figure C.4)

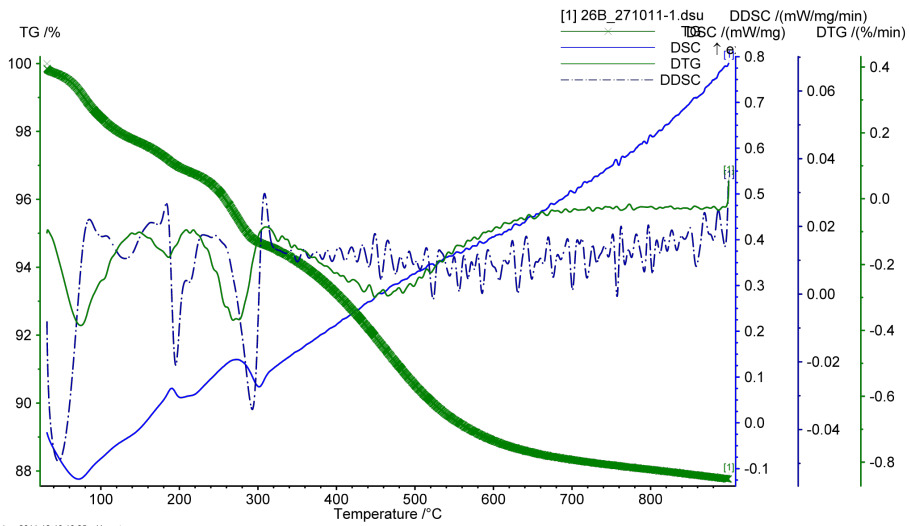


Figure C.6: Reduction of sample 26B (20% Co).

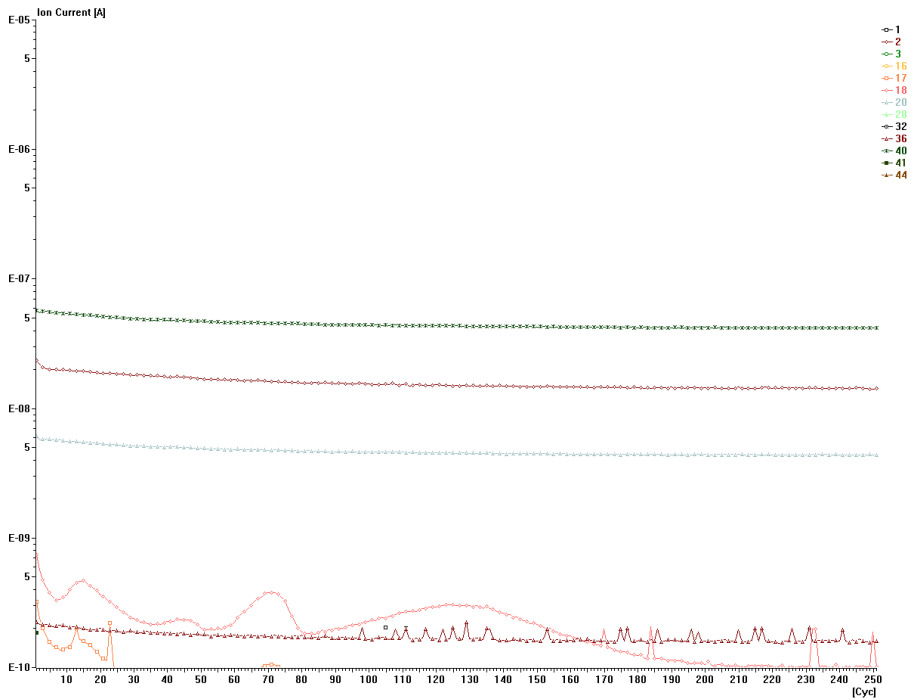


Figure C.7: Reduction of sample 26B (20% Co) (see figure C.6).

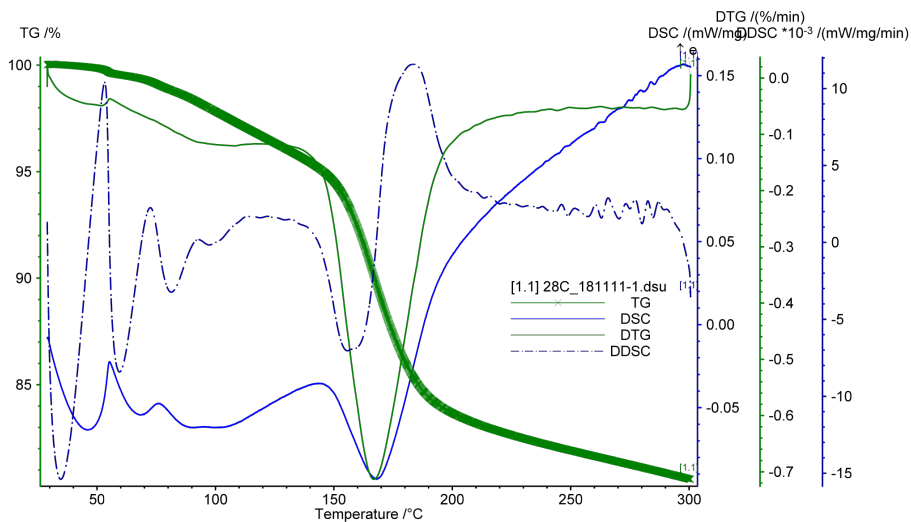


Figure C.8: Sample 28C (Uncalcinated catalyst) heated in an Ar-atmosphere.

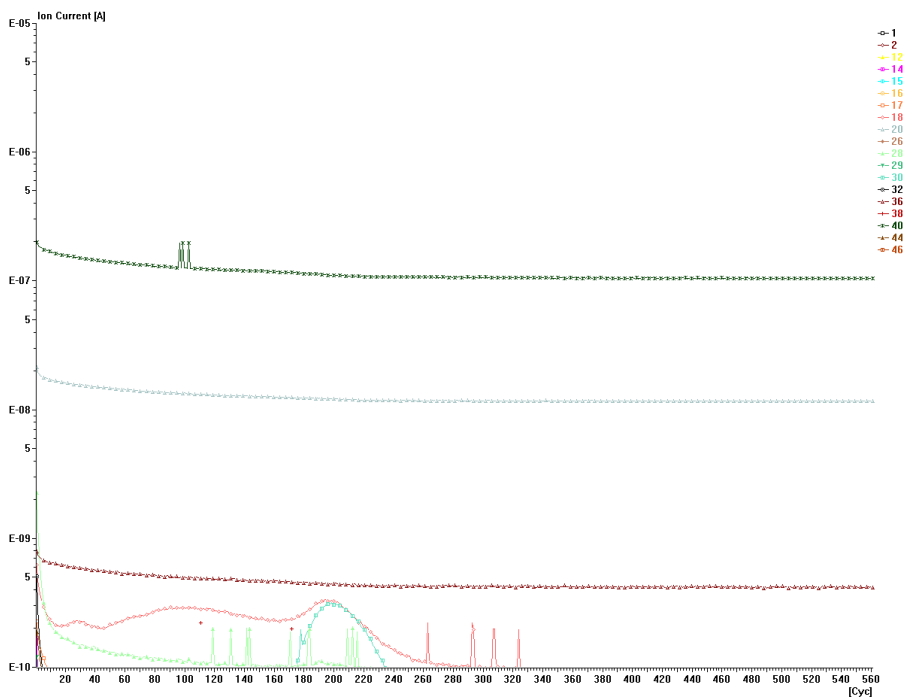


Figure C.9: Sample 28C (Uncalcinated catalyst) heated in an Ar-atmosphere (see figure C.8).

Table C.11: Dispersion and particle sizes measured by chemisorption

Sample	Composition	Dispersion	Est. particle size (d) [nm]
16D	20% Co, 5% Ni	6.37%	15.69
16D	20% Co, 5% Ni	8.26%	12.09
18D	20% Co, 1% Ni	6.54%	15.24
18D	20% Co, 1% Ni	6.99%	14.26
19B	6.3% Ni	26.64%	3.80
19B	6.3% Ni	29.52%	3.43
19D	20% Co, 5% Ni	8.46%	11.82
19D	20% Co, 5% Ni	8.19%	12.21
20D	20% Co, 1% Ni	7.97%	12.51
20D	20% Co, 1% Ni	7.59%	13.15
21D	20% Co, 10% Ni	8.56%	11.71
21D	20% Co, 10% Ni	8.44%	11.87
22B	20% Co	6.46%	15.43
22B	20% Co	7.22%	13.81
23D	20% Co, 5% Ni	8.23%	12.15
23D	20% Co, 5% Ni	8.40%	11.89
25B	20% Co, 10% Ni	6.77%	14.79
26B	20% Co	7.01%	14.21
26B	20% Co	7.01%	14.22
27B	10% Ni	22.88%	4.42
28D	10% Co, 1% Ni	7.33%	13.62
30D	20% Co, 10% Ni	8.59%	11.67
30D	20% Co, 10% Ni	8.79%	11.39
31B	11% Co, 5% Ni	8.62%	11.62
33B	20% Co	6.69%	14.89

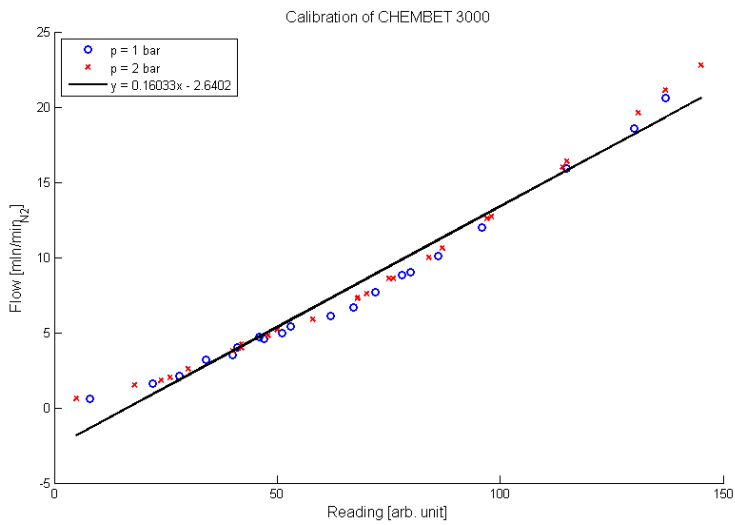


Figure C.10: Calibration curve for flowmeter, CHEMBET 3000

# Appendix D

## Risk assesment

The compulsory risk assesment for the thesis is attached in this appendix. The risk assesment has been updated multiple times during the laboratory work, and the dating refers to the date of the latest revision. Unlike the rest of the thesis, the risk assesment has been carried out in norwegian and not translated of reasons that NTNU uses different gradings to assess risk in forms written in english and norwegian language.



NTNU	Kartlegging av risikofylt aktivitet		Utarbeidet av	Nummer	Dato
			HMS-avd.	HMSRV2601	05.03.2010
HMS			Godkjent av	Side	Erstatter
			Rektor	1 av 2	01.12.2006

Enhet: IKP

Deltakere ved kartleggingen (m/ funksjon): Vegar Evenrud, stud.techn.

Dato: 05.02.2012

### Kort beskrivelse av hovedaktivitet/hovedprosess:Framstilling og karakterisering av heterogene katalysatorer

ID nr.	Aktivitet/prosess	Ansvarlig	Lov, forskrift o.l.	Eksisterende dokumentasjon	Eksisterende sikringstiltak	Kommentar
1	Impregnering (framstilling av katalysator)	Vegar Evenrud	-	HMS-datablader for $\text{Co}(\text{NO}_3)_2 \cdot 6\text{H}_2\text{O}$ og $\text{Ni}(\text{NO}_3)_2 \cdot 6\text{H}_2\text{O}$	Avtrekk	
2	Tøking under vakuum (framstilling av katalysator)	Vegar Evenrud	-	-	Avtrekk og beskyttelseskabinett	
3	Kalsinering (framstilling av katalysator)	Vegar Evenrud	-	-	Avtrekk	
4	Røntgendiffraksjonsmåling (karakterisering)	Julian Tolchard	-	-	Apparatur sikret mot bruk detsom det ikke er lukket.	
5	Temperaturprogrammert reduksjonsmåling (karakterisering)	Rune Lødeng	-	-	Gassdetektor	Lukket system
6	Kjemisorpsjon (karakterisering)	Magnus Rønning	-	-	Gassdetektor	Lukket system
7	Fysisorpsjon (karakterisering)	Julian Tolchard	-	-	-	
8	TGA (karakterisering)	Magnus Rønning	-	-	Gassdetektor	Lukket system

Hva

NTNU	Kartlegging av risikofylt aktivitet			Utarbeidet av	Nummer	Dato
				HMS-avd.	HMSRV2601	05.03.2010
HMS				Godkjent av	Side	Erstatter
				Rektor	2 av 2	01.12.2006



### Aktivitet/prosess

Kartlegging av aktiviteter/prosesser som inngår i risikovurderingen og som kan inneha risiko for skade på menneske eller miljø. Dette kan f.eks. være maskiner, labaktivitet, verkstedarbeid, bruk av visse kjemikalier osv. Bryt ned hele aktiviteten/prosessen i enkeltdele, beskriv kort hver del.

Aktivitetene velges enten som gjennomgang av en prosess (aktivitet fra f.eks. innkjøp av materiale, via bearbeiding til ferdig produkt), eller alle aktiviteter som oppleves mulig risikofylte i et gitt område. Deltagerne må bli enige om omfanget av aktivitetene som skal risikovurderes,

Man må ta stilling til

- "Risiko for hvem" - for ansatte, for nabomiljø, for enkeltindivider eller en gruppe, for bedriften, for samfunnet
- "Risiko fra hva" - hvilket anlegg, hvilken aktivitet, fra hvilke ulykkeskategorier
- "For hvilket tidsrom"- risikonivået kan variere over tid

Risiko er et potensielt tap, ikke et oppstått tap. Aktiviteter/prosesser som i utgangspunktet blir vurdert som lite risikofylte, kan medføre økt risiko under gitte forhold.

### Ansvarlig

Hvem er ansvarlig for de enkelte aktiviteter/prosesser? Er det noen andre enheter som har ansvar eller oppgaver for å redusere risiko? Organisasjonskart kan brukes for å avklare ansvarsforhold

### Lov, forskrift o.l.

Hvilke lover, forskrifter og andre myndighetskrav gjelder for aktiviteten/prosessen? Se HMS-håndboka, [HMSRV-20/01](https://www.hmsrv-20/01), [www.lovdataba.no](http://www.lovdataba.no), [www.arbeidstilsynet.no](http://www.arbeidstilsynet.no), [www.hmsetatene.no](http://www.hmsetatene.no), kommunale bestemmelser ([www.trondheim.kommune.no](http://www.trondheim.kommune.no))

### Eksisterende dokumentasjon

Enheten skal finne fram eksisterende sentrale og lokale retningslinjer, tegningsunderlag, sertifikater, krønerbevis, truckførerbevis, gjennomført opplæring, serviceavtaler, bruksanvisninger, sjekklister osv. Se også tidligere risikovurderinger og HMS-runder, lokalt HMS-hefte, labhåndbok, [NTNUs.stoffkartotek](http://NTNUs.stoffkartotek) osv.

### Sikringstiltak

Hva finnes av eksisterende sikringstiltak for området/utstyret? Feks. ventilasjon, personlig verneutstyr, nødstop, merking/tilting, skillevegger osv.

NTNU

HMS/KS

## Risikovurdering

utarbeidet av	Nummer	Dato
HMS-avd.	HMSRY2603	4.3.2010
godkjent av	side	Erstatter
Rektor	1 av 2	9.2.2010



Enhet: IKP

Linjeleder: Magnus Rønning

Deltakere ved risikovurderingen (m/ funksjon): Vegar Evenrud, stud.techn.

Dato: 05.02.2012

ID nr	Aktivitet fra kartleggings-skjemaet	Mulig uønsket hendelse/ belastning	Vurdering av sannsynlighet (1-5)	Vurdering av konsekvens:				Risiko-verdi	Kommentarer/status Forslag til tiltak
				Menneske (A-E)	Ytre miljø (A-E)	Øk/ materiell (A-E)	Om-dømm (A-E)		
1	Impregnering	Senskader ved eksponering ovenfor metaller	1	D	-	-	-	D1	Bruke hansker ved håndtering. Unngå innånding av partikler samt oralt inntak.
2	Impregnering	Eksponering ovenfor nitrose gasser ved tørking.	3	B	-	-	-	B3	Tørk under avtrekkspunkt
3	Tørking under vakuum	Kuttskader ved implosjon	2	B	-	-	-	B2	Bruke vernebriller. Hold beskyttelseskabinettet lukket og begrenns berøring av glassutstyr.
4	Tørking under vakuum	Eksponering ovenfor nitrose gasser	2	B	-	-	-	B2	Sørg for at vakuumpumpa er koblet til avtrekk
5	Kalsinering	Brannskade ved berøring av varmt utstyr	3	A	-	-	-	A3	Unngå å berøre varmt utstyr
6	Kalsinering	Eksponering ovenfor nitrose gasser	3	B	-	-	-	B3	Sørg for at avtrekk er åpent og tilkoblet. Unngå oppsamling av utfelling i nitratfelle.
7	Temperaturprogrammer t reduksjonsmåling	Brannskade ved berøring av varmt utstyr	3	A	-	-	-	A3	Unngå å berøre varmt utstyr
8	Temperaturprogrammer t reduksjonsmåling	Kuttskader gitt av skjørt glassutstyr	3	A	-	-	-	A3	Utvise forsiktighet ved fylling, tømming og skifte av reaktor
9	Kjemisorpsjon	Brannskade ved berøring av varmt utstyr	3	A	-	-	-	A#	Unngå å berøre varmt utstyr

NTNU		Risikovurdering		utarbeidet av		Nummer		Dato	
 HMS/IKS				HMS-avd.		HMSRY2603		4.3.2010	
				godkjent av		side		Erstatter	
		Rektor		2 av 2		9.2.2010			

Aktivitet fra kartleggings-skjemaet	Mulig uønsket hendelse/belastning	Vurdering av sannsynlighet	Vurdering av konsekvens:			Risiko-verdi	Kommentarer/status Forslag til tiltak
			1	2	3		
10	Brannskade ved lekkasje og antennelse av brennbar gass	1	D	-	-	D1	Unngå bruk dersom det er synlige skader på utstyr.
11	Frostskader ved kontakt med flytende nitrogen	3	B	-	-	B3	Utvis forsiktighet ved håndtering og transport
12	TGA	1	D	-	-	D1	Unngå bruk dersom det er synlige skader på utstyr.

**Sannsynlighet**

1. Svært liten
2. Liten
3. Middels
4. Stor
5. Svært stor

**Risikoverdi (beregnes hver for seg):**

- Menneske** = Sannsynlighet x Konsekvens  
**Ytre miljø** = Sannsynlighet x Konsekvens  
**Økonomi/materiell** = Sannsynlighet x Konsekvens  
**Omdømme** = Sannsynlighet x Konsekvens

**Sannsynlighet vurderes etter følgende kriterier:**

Svært liten 1	Liten 2	Middels 3	Stor 4	Svært stor 5
1 gang pr 50 år eller sjeldnere	1 gang pr 10 år eller sjeldnere	1 gang pr år eller sjeldnere	1 gang pr måned eller oftere	Skjer ukentlig

**Konsekvens vurderes etter følgende kriterier:**

Gradering	Menneske	Ytre miljø Vann, jord og luft	Øk/materiell	Omdømme
E Svært Alvorlig	Død	Svært langvarig og ikke reversibel skade	Drifts- eller aktivitetsstans >1 år.	Troverdighet og respekt betydelig og varig svekket

## Risikovurdering

	Alvorlig personskade. Mulig uførhet.	Langvarig skade. Lang restitusjonstid	Driftsstans > ½ år Aktivitetstans i opp til 1 år	Troverdighet og respekt betydelig svekket
<b>D</b> Alvorlig	Alvorlig personskade.	Langvarig skade. Lang restitusjonstid	Driftsstans > ½ år Aktivitetstans i opp til 1 år	Troverdighet og respekt betydelig svekket
<b>C</b> Moderat	Alvorlig personskade.	Mindre skade og lang restitusjonstid	Drifts- eller aktivitetstans < 1 mnd	Troverdighet og respekt svekket
<b>B</b> Liten	Skade som krever medisinsk behandling	Mindre skade og kort restitusjonstid	Drifts- eller aktivitetstans < 1uke	Negativ påvirkning på troverdighet og respekt
<b>A</b> Svært liten	Skade som krever førstehjelp	Ubetydelig skade og kort restitusjonstid	Drifts- eller aktivitetstans < 1dag	Liten påvirkning på troverdighet og respekt

### Risikoverdi = Sannsynlighet x Konsekvens

Beregn risikoverdi for Menneske. Enheten vurderer selv om de i tillegg vil beregne risikoverdi for Ytre miljø, Økonomi/materiell og Omdømme. I så fall beregnes disse hver for seg.

### Til kolonnen "Kommentarer/status, forslag til forebyggende og korrigerende tiltak":

Tiltak kan påvirke både sannsynlighet og konsekvens. Prioriter tiltak som kan forhindre at hendelsen inntreffer, dvs. sannsynlighetsreducerende tiltak foran skjerpet beredskap, dvs. konsekvensreducerende tiltak.